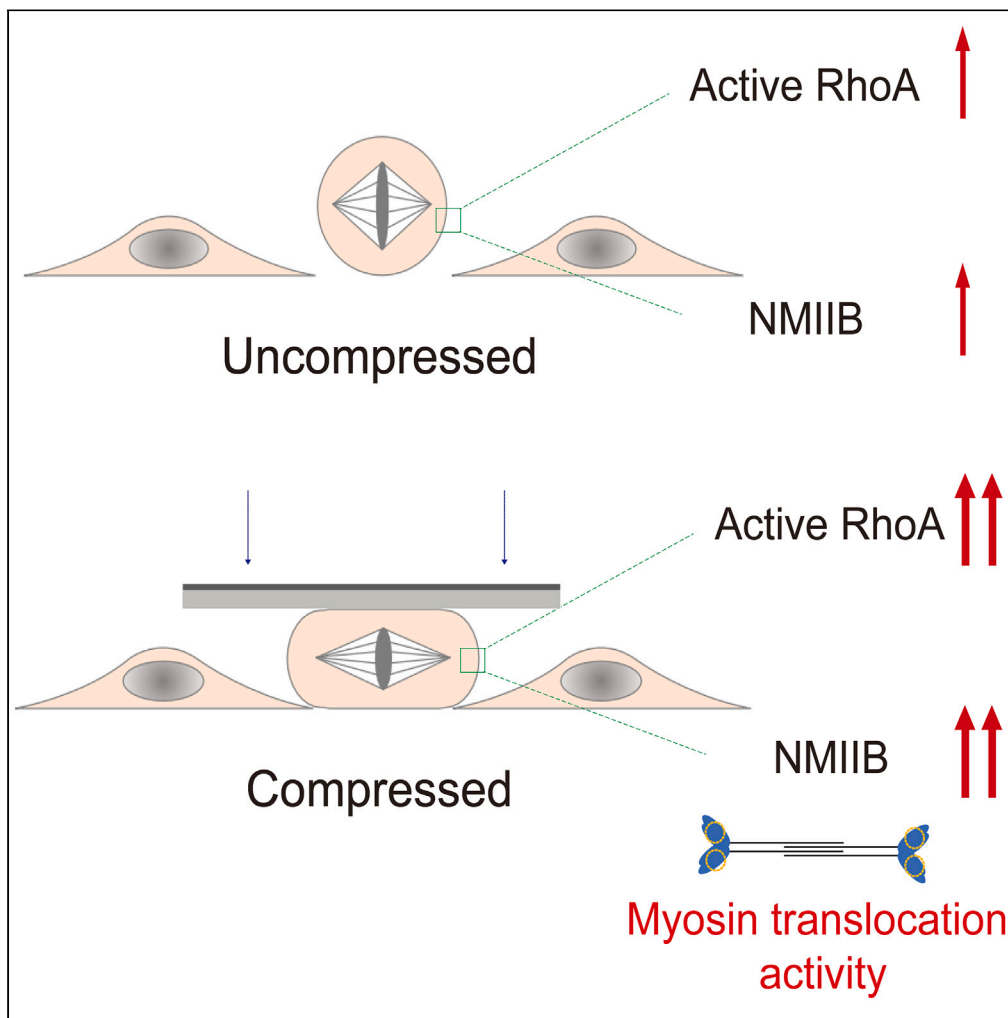# iScience

Article

Mechanosensitive accumulation of non-muscle myosin IIB during mitosis requires its translocation activity

Chao Wang,
Jingjing Ding,
Qiaodong Wei,
Shoukang Du,
Xiaobo Gong, Ting
Gang Chew

tinggchew@intl.zju.edu.cn

Highlights

RhoA and NMIIB display
mechanosensitive
accumulation at the mitotic
cell cortex

Mitotic NMIIB
mechanoresponse involves
regulation by RhoA/ROCK
signaling

The translocation activity of
NMIIB head domain is
required for its
mechanoresponse

Article

Mechanosensitive accumulation of non-muscle myosin IIB during mitosis requires its translocation activity

Chao Wang,[1,2,4] Jingjing Ding,[1,2,4] Qiaodong Wei,[3] Shoukang Du,[1,2] Xiaobo Gong,[3] and Ting Gang Chew[1,2,5,*]

SUMMARY

Non-muscle myosin II (NMII) is a force-generating mechanosensitive enzyme that responds to mechanical forces. NMIIs mechanoaccumulate at the cell cortex in response to mechanical forces. It is essential for cells to mechanically adapt to the physical environment, failure of which results in mitotic defects when dividing in confined environment. Much less is known about how NMII mechanoaccumulation is regulated during mitosis. We show that mitotic cells respond to compressive stress by promoting accumulation of active RhoA at the cell cortex as in interphase cells. RhoA mechanoresponse during mitosis activates and stabilizes NMIIB via ROCK signaling, leading to NMIIB mechanoaccumulation at the cell cortex. Using disease-related myosin II mutations, we found that NMIIB mechanoaccumulation requires its motor activity that translocates actin filaments, but not just its actin-binding function. Thus, the motor activity coordinates structural movement and nucleotide state changes to fine-tune actin-binding affinity optimal for NMIIs to generate and respond to forces.

INTRODUCTION

Non-muscle myosin IIs (NMIIs) are a family of actin-based molecular motors that function with actin filaments to generate forces to drive cell morphogenesis, cell migration, and cell division.[1,2] NMIIs and actin filaments form a layer of contractile cytoskeletal network at the cell cortex to function as the main mechanical element to drive changes of cell shape during mitosis.[3,4] Upon entry into mitosis, actin filaments assemble into a network architecture that is thin and penetrable for NMIIs to generate the cell cortex with high tension to counteract high intracellular hydrostatic pressure.[5–7] This facilitates mitotic cell rounding in cells transiting from interphase into mitosis and sustains a round cell shape throughout mitosis.[8–10] Cells that are not able to maintain a round cell shape when dividing in a physically confined environment have defects in their mitotic spindle stability and form multipolar spindles that lead to chromosome mis-segregation and aneuploidy.[11–13]

As cells enter mitosis, activation of cyclin-dependent kinase 1 (CDK1) triggers the cytoplasmic shuttling of a Rho guanine nucleotide exchange factor (RhoGEF) Ect2 to activate RhoA, which in turn binds to the cell membrane and recruits its effectors such as anillin, formin and Rho-associated kinase (ROCK). This leads to activation of NMIIs to slide on actin filaments that are homeostatically maintained at the cell cortex.[9,14–17] Activation of this signaling cascade results in generation of higher cell surface tension, which leads to mitotic cell rounding crucial in providing an ideal cell geometry to undergo mitosis and cytokinesis.[7,12,18]

NMII consists of two heavy chains, two regulatory light chains (MRLC) and two essential light chains (ELC). The myosin heavy chain has a globular head, a flexible neck structure and an elongated tail region.[19] NMII is activated when the neck structure is bound by MRLC phosphorylated via RhoA-mediated ROCK signaling.[20,21] Further phosphoregulation of the myosin tail region assembles active NMIIs into multimeric myofilaments that have high affinity to actin filaments.[21,22] The motor activity in the globular head of myofilaments catalyses nucleotide hydrolysis to form the cross-bridge and to translocate actin filaments via lever arm movement.[19] Apart from force generation, NMIIs sense and respond to mechanical inputs in cells. In response to mechanical forces, NMIIs accumulate at the cell cortex of the stressed region in cells.[23] The three mammalian NMII paralogs (NMIIA, NMIIB, NMIIC) accumulate at the region that is mechanically stressed (mechanoaccumulation), with NMIIB showing differential mechanoresponse across cell types and cell cycle phases.[24] Mechanoaccumulation of NMIIs is influenced by the length of its neck structure in which an extended length of the neck structure facilitates its accumulation.[23] Furthermore, phosphoregulation of NMII's tail region that modulates myofilament assembly states contributes to the ability of NMIIs to accumulate at the cell cortex in response to mechanical stress.[25]

[1]Department of Cardiology of the Second Affiliated Hospital, Zhejiang University School of Medicine, Zhejiang University, Hangzhou 310058, China
[2]The Zhejiang University-University of Edinburgh Institute, Zhejiang University School of Medicine, Zhejiang University, Haining 314400, China
[3]Department of Engineering Mechanics, School of Naval Architecture, Ocean and Civil Engineering, Shanghai Jiao Tong University, Shanghai 200240, China
[4]These authors contributed equally
[5]Lead contact
*Correspondence: tinggchew@intl.zju.edu.cn
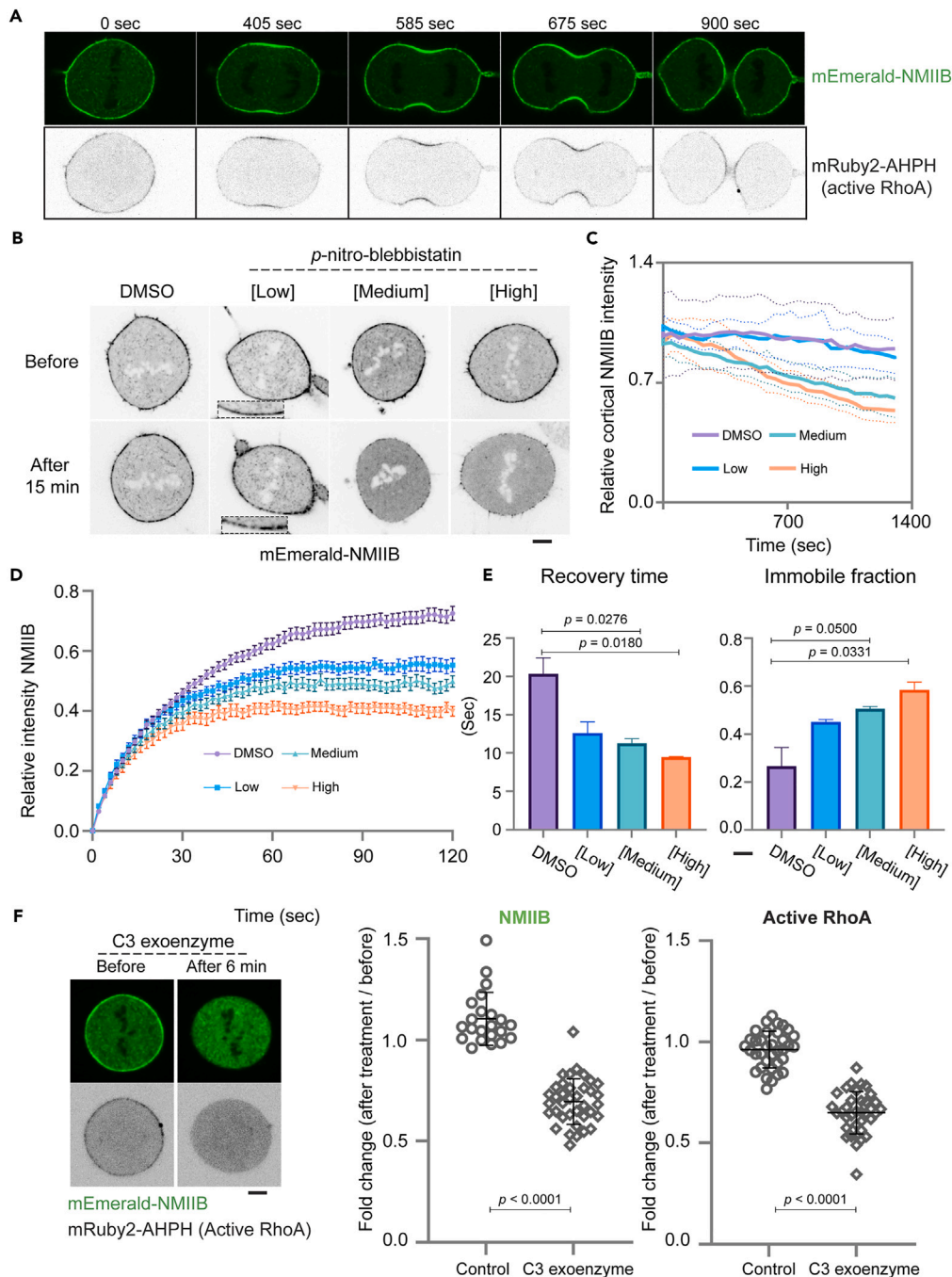https://doi.org/10.1016/j.isci.2023.107773

Figure 1. Establishment of a MCF10A cell line stably expressing mEmerald-NMIIB and mRuby2-AHPH (active RhoA)

(A) Micrographs of a representative cell showing mEmerald-NMIIB and active RhoA localization during mitosis and cytokinesis.

(B) Micrographs of the cortical mEmerald-NMIIB in mitotic cells treated with different concentrations of *p*-nitroblebb. Cells before and 15 min after the treatments were shown. [Low] is 37 µM; [Medium] is 74 µM; [High] is 110 µM. Insets show a zoom-in view of the punctate NMIIB.

(C) Relative changes of cortical NMIIB intensity as a function of time. The fluorescence intensity at each time point was normalized to that of in cells before treatments. Dotted lines indicate standard deviation. DMSO, 12 cells; low, 9 cells; medium, 9 cells; high, 10 cells.

(D) Recovery curves of mEmerald-NMIIB fluorescence intensity after photobleaching in cells treated with different concentrations of *p*-nitroblebb. DMSO, 36 cells; low, 36 cells; medium, 30 cells; high, 28 cells.

(E) Quantification of the recovery time and the immobile fraction of mEmerald-NMIIB by FRAP.

Figure 1. Continued

(F) Effect of C3 exoenzyme treatment on the cortical NMIIB and active RhoA in a mitotic cell is shown. The changes of NMIIB and active RhoA intensities at the mitotic cell cortex before and after 10 μg/mL C3 exoenzyme treatments were quantified. The fold change is a ratio of the mean intensity after 10 μg/mL C3 exoenzyme treatment to the mean intensity before treatment. The control group was added with media as C3 exoenzyme was dissolved in water. NMIIB (control), 22 cells; NMIIB (C3 exoenzyme), 37 cells; active RhoA (control), 35 cells; active RhoA (C3 exoenzyme), 36 cells. Data represent means ± SD. Data were collected from 3 independent experiments. Scale bar, 5 μm.

Much has been done to understand the force generation mechanism of NMIIs, less is known about how NMII's mechanoresponse is regulated. In this study, we aimed to understand the mechanism for NMIIB mechanoaccumulation in mitotic cells responding to compressive forces. It has been previously shown that interphase cells cultured in 3D matrixes activates RhoA and NMIIs in response to compression.[26] By using a cell contractility reporter cell line, we found that cells respond to compressive stress during mitosis by accumulating active RhoA at the cell cortex, which in turn leads to higher activation and mechanoaccumulation of NMIIB. Interestingly, further genetic dissection of NMIIB head domain by using mutations that uncouple actin-binding function and motor activity to translocate actin filaments showed that the translocation activity of NMIIB plays a primary role for its ability to undergo mechanoaccumulation. We propose that the NMIIB translocation activity coordinates structural changes to nucleotide state changes to prepare NMIIBs of differential actin-binding affinity, so to achieve mechanoaccumulation at the cell cortex in response to compressive forces during mitosis.

RESULTS

Construction and validation of a cell contractility reporter cell line

To study how NMII mechanoresponse is regulated during mitosis, we made a human MCF10A mammary epithelial cell stably expressing fluorescently tagged non-muscle myosin IIB (mEmerald-NMIIB) and active RhoA reporter consisting of the RhoA-binding domain of anillin (mRuby2-AHPH).[27–31] NMIIB localizes to the cell cortex in the early mitosis and functions downstream of active RhoA to generate cortical tension.[15,32] Live-cell microscopy imaging revealed that NMIIB and active RhoA localized to the cell cortex starting from early mitosis and enriched at the division site during mitosis and cytokinesis, consistent with previous studies and their roles in tension generation at the cell cortex during cell division (Figure 1A).[15,28,32] To examine the activity of mEmerald-NMIIB, we treated mitotic cells with low, medium and high concentrations of the low cytotoxic and photostable NMII inhibitor para-nitroblebbistatin (p-nitroblebb), which lowers the actin affinity of NMII heads.[33,34] Mitotic cells treated with a low concentration of p-nitroblebb showed punctate cortical NMIIB patterns (Figure 1B, insets). Higher concentrations of p-nitroblebb resulted in a decreasing NMIIB intensity at the mitotic cell cortex (Figures 1B and 1C). Analyses of the NMIIB turnover at the mitotic cell cortex with the fluorescence recovery after photo bleaching technique (FRAP) showed an increase of the immobile fractions of NMIIB upon increased concentrations of p-nitroblebb (Figures 1D and 1E; DMSO: 0.27 ± 0.08; [Low]: 0.45 ± 0.01; [Medium]: 0.50 ± 0.01; [High]: 0.59 ± 0.03). The recovery half-time of cortical NMIIB decreased when increasing concentrations of p-nitroblebb were used (Figure 1E; DMSO: 20.33 ± 2.09 s; [Low]: 12.61 ± 1.46 s; [Medium]: 11.30 ± 0.59 s; [High]: 9.49 ± 0.05 s). The FRAP analysis suggested that a decrease of NMIIB recovery half-time with higher immobile fractions characterizes inhibition of mEmerald-NMIIB function at the cell cortex by the NMII inhibitor.

To test the response of active RhoA reporter, mitotic cells were treated with a RhoA inhibitor C3 exoenzyme that prevents activation of RhoA, both active RhoA and NMIIB disappeared from the mitotic cell cortex (Figure 1F). This indicates that mRuby2-AHPH reliably reports the active state of RhoA. Taken together, AHPH-mRuby2 and mEmerald-NMIIB report the status of cellular contractility during mitosis and cytokinesis.

Mechanoaccumulation of NMIIB and active RhoA at the mitotic cell cortex

To study how NMIIB responds to mechanical forces during mitosis, we compressed the mitotic cells with a soft elastic gel and a weight (Figure 2A). When compressive forces were exerted on the mitotic cells, the cell has enlarged its diameter, and the cell height has decreased from 22.89 ± 1.88 μm to 15.19 ± 1.19 μm (Figures 2B and 2C). Within 2 min after compression, we observed increased intensity of NMIIB at the mitotic cell cortex. In average, there was 1.45 ± 0.29-fold increase of cortical NMIIB intensity in individual cells (Figures 2D and 2E). Concomitantly, active RhoA increased its intensity at the mitotic cell cortex by 1.54 ± 0.31-fold compared to that of before compression (Figure 2F). Approximately 76.5% individual cells showed an increase of both active RhoA and NMIIB at the mitotic cell cortex after compression (Figure S1A), suggesting that in response to compressive forces, mitotic cells accumulate more active RhoA leading to an accumulation of NMIIB at the cell cortex. Consistently, individual mitotic cells expressing active RhoA reporter using Rhotekin Rho binding domain[35] also showed mechanoaccumulation of active RhoA at the cell cortex in response to compressive forces (Figure S1B). A cell membrane-localized protein did not significantly increase its intensity at the cell membrane upon compression, suggesting that the mechanical response is specific to active RhoA and NMIIB (Figure S1C). Furthermore, compressive forces have resulted in more activated NMII as revealed by higher level of phosphorylated myosin regulatory light chain (p-MRLC) in the cell lysate from compressed cells (Figure S1D). Previous studies showed that compressive stress activates RhoA and NMIIs in interphase cells grown in 3D matrixes.[26] We compressed rounded interphase cells using our approach and similarly observed increased intensity of active RhoA and NMIIB at the cell cortex (Figure S1E), indicating mechanoresponsiveness of active RhoA and NMIIB in both interphase and mitotic cells.

To test whether mechanoaccumulation of active RhoA at the cell cortex depends on cell surface tension, we decreased cell surface tension by inhibiting NMII function with p-nitroblebb treatment. We first measured cell surface tension in mitotic cells treated with p-nitroblebb using
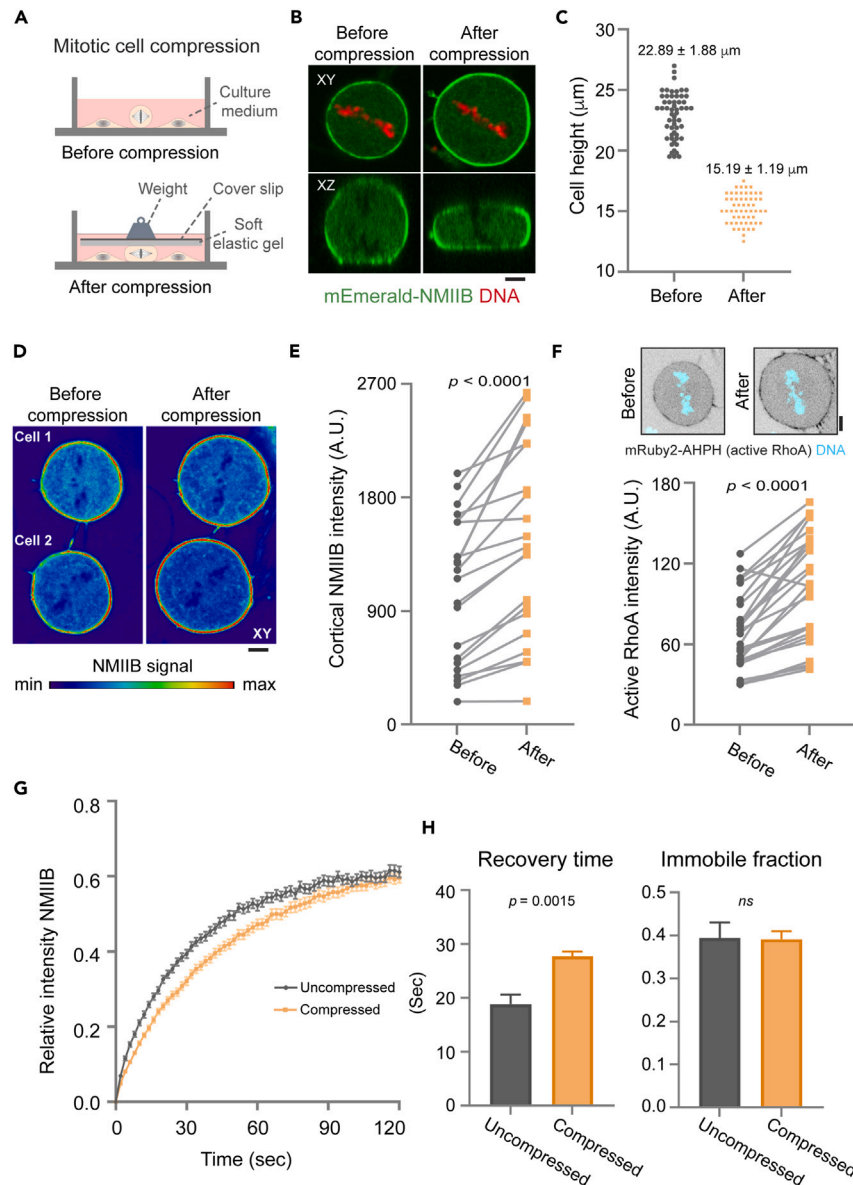
Figure 2. NMIIB and active RhoA show mechanoaccumulation at the cell cortex during mitosis

(A) A schematic representation of the mitotic cell compression experiment. A soft elastic polyacrylamide gel (2 kPa) was used in the study.

(B) A representative cell before and after compression is shown. XY, top view; XZ, side view.

(C) Quantification of the cell height before and after compression. 56 cells were counted for their cell height before and after compression.

(D) Two representative cells with increased accumulation of NMIIB at the cell cortex are shown.

(E) Intensity of the cortical NMIIB in mitotic cells before and after compression was quantitated. Black dots indicate the intensity before compression and orange dots indicate the intensity after compression of the same cells. 21 cells were counted.

(F) Intensity of active RhoA in mitotic cells before and after compression was quantitated. Black dots indicate the intensity before compression and orange dots indicate the intensity after compression of the same cells. A representative cell with increased cortical active RhoA after compression is shown. 26 cells were counted.

(G) Recovery curves of the cortical mEmerald-NMIIB intensity in uncompressed cells and in compressed cells after photobleaching. Uncompressed, 55 cells; compressed, 48 cells.

(H) Quantification of the recovery time and the immobile fraction of mEmerald-NMIIB by FRAP. Data represent means ± SD, except for (G) where data represent ±SEM. Data were collected from 3 independent experiments. Scale bar, 5 μm. See also Figures S1 and S2.

A

DMSO | Y-27632 | RO-3306

Before compression | After compression | Before compression | After compression | Before compression | After compression

CDK1 (RO-3306)
|
RhoGEF
|
RhoA
|
ROCK (Y-27632)
|
Actomyosin

mEmerald-NMIIB   mRuby2-AHPH (Active RhoA)

B — DMSO / Y-27632: Cortical NMIIB intensity (A.U.), $p < 0.0001$

DMSO / Y-27632: Active RhoA intensity (A.U.), $p < 0.0007$ / $p < 0.0001$

C — Fold change (after compression and Y-27632 treatment / before)

NMIIB: $p < 0.0001$; Active RhoA: $p = 0.7831$

D — DMSO / RO-3306: Cortical NMIIB intensity (A.U.), $p < 0.0001$

DMSO / RO-3306: Active RhoA intensity (A.U.), $p < 0.0001$

E — Fold change (after compression and RO-3306 treatment / before)

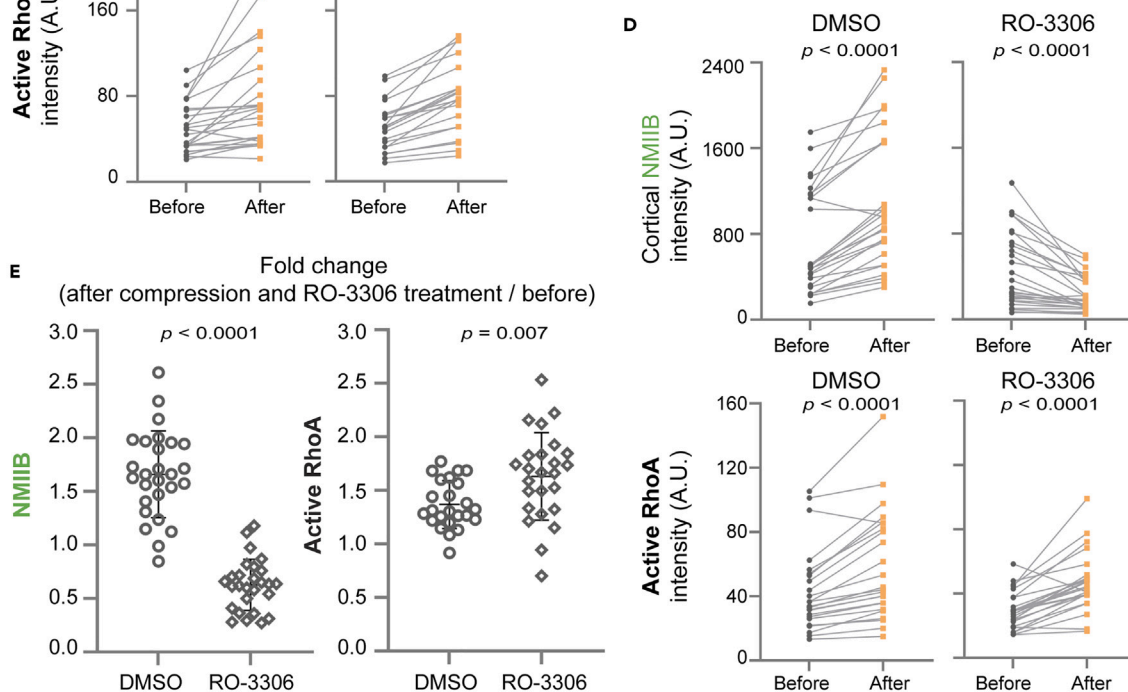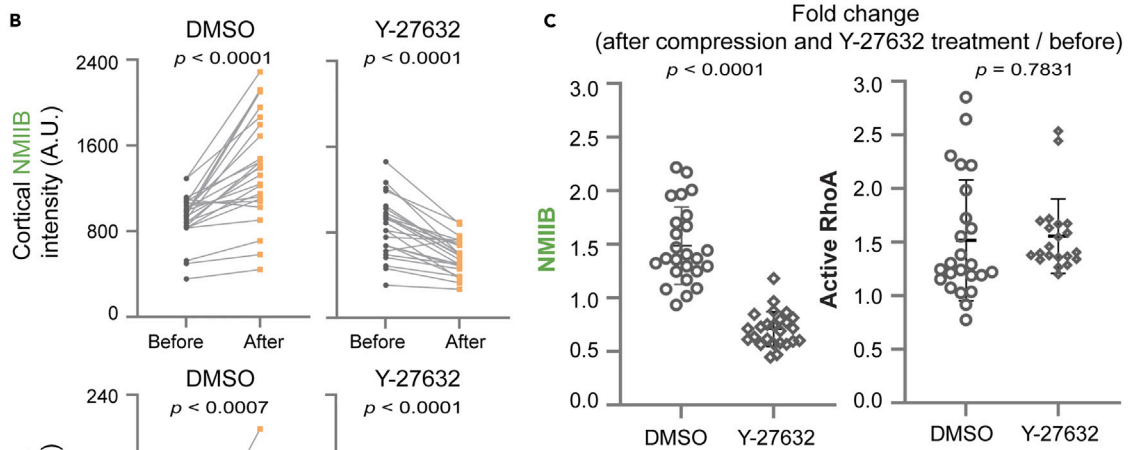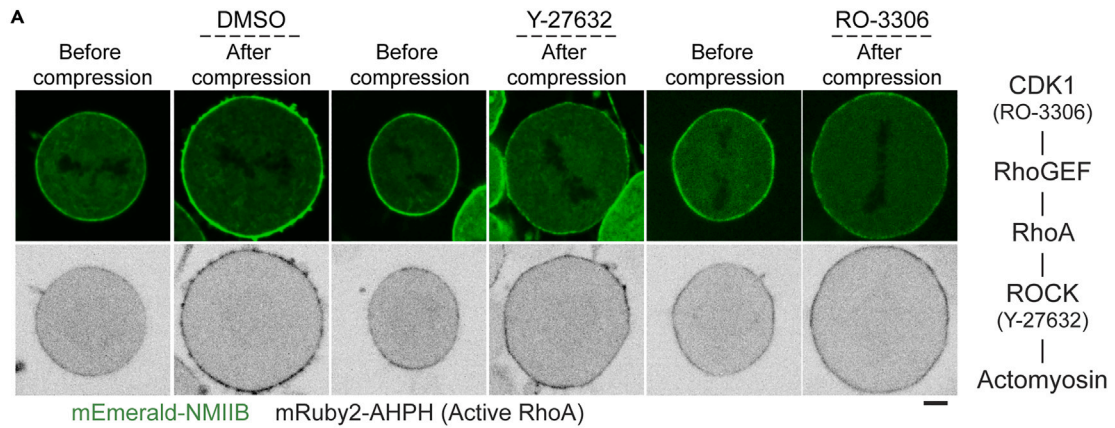NMIIB: $p < 0.0001$; Active RhoA: $p = 0.007$

Figure 3. Regulation of NMIIB mechanoresponse by ROCK and CDK1 signaling pathways

(A) The cortical NMIIB and active RhoA at the cell cortex of mitotic cells before and after DMSO or 20 μM Y-27632 treatments or 10 μM RO-3306 are shown.

(B) Quantification of the changes of NMIIB and active RhoA intensities at the cell cortex before and after DMSO or 20 μM Y-27632 treatments.

(C) The fold change is a ratio of the mean intensity after treatments to the mean intensity before treatment. A ratio higher than 1 means a positive mechanoresponse. NMIIB (DMSO), 26 cells; NMIIB (Y-27632), 47 cells; active RhoA (DMSO), 30 cells; active RhoA (Y-27632), 55 cells.

(D) Quantification of the changes of NMIIB and active RhoA intensities at the cell cortex before and after DMSO or 10 μM RO-3306 treatments.

(E) The fold change is a ratio of the mean intensity after treatments to the mean intensity before treatment. A ratio higher than 1 means a positive mechanoresponse. NMIIB (DMSO), 27 cells; NMIIB (RO-3306), 27 cells; active RhoA (DMSO), 24 cells; active RhoA (RO-3306), 25 cells. Data represent means ± SD. Data were collected from 3 independent experiments. Scale bar, 5 μm. See also Figures S3 and S4.

the micropipette aspiration technique. The mitotic cell surface tension decreased to 56%, 44%, 31% of the control group after treatments with low, medium and high concentrations of *p*-nitroblebb, respectively (Figure S2A; DMSO: 894.90 ± 186.74 pN/μm; [Low]: 500.42 ± 90.64 pN/μm; [Medium]: 393.87 ± 121.08 pN/μm; [High]: 281.58 ± 60.84 pN/μm). Upon *p*-nitroblebb treatment, we observed that the cortical localization of active RhoA decreased when cell surface tension has been lowered for 3-fold in mitotic cells treated with *p*-nitroblebb, suggesting that RhoA could respond to the cortical tension generated by NMII during mitosis (Figure S2B).

Next, we used FRAP to analyze the cortical NMIIB turnover in mitotic cells under compression. We found that compression in mitotic cells has slowed down the turnover of the cortical NMIIB, with an increase of the recovery half-time of 27.75 ± 0.86 s as compared to that of in the uncompressed mitotic cells that was 18.85 ± 1.79 s (Figures 2G and 2H). Thus, compressive forces stabilize NMIIB at the mitotic cell cortex leading to mechanoaccumulation of NMIIB.

Roles of RhoA/ROCK and CDK1 in mitotic NMIIB mechanoaccumulation under compression

When cells are entering mitosis from G2 phase, cyclin-dependent kinase 1 (CDK1) regulates RhoGEF Ect2 to activate RhoA, which in turn exerts its effects on the actomyosin network to generate forces through ROCK signaling (Figure 3A).[14,17] Since we found that active RhoA responds to compressive forces during mitosis and leads to NMIIB activation and accumulation at the cell cortex, we asked whether CDK1 and ROCK are involved in the mechanoaccumulation of RhoA and NMIIB during mitosis. We first examined the effects of CDK1 and ROCK inhibition in mitotic cells not subjected to compressive forces. When mitotic cells were chemically inhibited by the ROCK inhibitor Y-27632, NMIIB decreased about 2-fold at the cell cortex while active RhoA did not show significant changes, which is consistent with NMIIB functions downstream of ROCK following RhoA activation (Figures S3A and S3B). Consistently, there was about 20% decrease of cell surface tension from 965.34 ± 133.34 pN/μm in the control group to 770.04 ± 160.08 pN/μm in the Y-27632 treated group (Figure S3C). Of note, a decrease of cell surface tension by the concentration of Y-27632 used in this study was not sufficient to reduce active RhoA from the cell cortex. When we treated mitotic cells with CDK1 inhibitor RO-3306, NMIIB decreased about 2-fold at the cell cortex and the cell surface tension decreased 15% to 821.67 ± 106.14 pN/μm compared to the control group (Figures S3A–S3D). Interestingly, active RhoA showed an increased accumulation at the cell cortex upon inhibition of CDK1 (Figures S3B). Thus, CDK1 appears to regulate NMIIB without RhoA activation in mitotic cells, which is different from that of in interphase cells entering mitosis.

To test if the RhoA/ROCK and CDK1 that regulate force generation of the actomyosin network were involved in mechanoresponse of NMIIB and RhoA, we compressed mitotic cells treated with ROCK or CDK1 inhibitors (Figures 3A and S4A). When mitotic cells were compressed for about 8 min in the presence of Y-27632, there was a decrease of cortical NMIIB as compared to the control group that showed an increase of cortical NMIIB after compression (Figures 3A–3C). Active RhoA accumulated at the mitotic cell cortex after compression in the presence or absence of Y-27632 (Figures 3A–C). Similarly, when mitotic cells were compressed in the presence of RO-3306 (Figure S3D), NMIIB decreased its intensity at the cell cortex while active RhoA showed mechanoaccumulation at the cell cortex (Figures 3A, 3D and 3E). We also observed an increase of active RhoA at the mitotic cell cortex after CDK1i treatment in cells expressing Rhotekin GBD as the active RhoA reporter (Figure S4B). It is to note that the cells were not exiting mitosis when cells were imaged for quantification after CDK1i treatment and compression. Since CDK1 regulates Ect2 to activate RhoA upon entry into mitosis, we knocked down Ect2 and observed that mitotic cells have slightly lower active RhoA and NMIIB at the cell cortex. However, upon compression, we observed increased active RhoA and NMIIB at the cell cortex (Figure S4C), suggesting that the CDK1/Ect2 signaling axis does not play an important role in controlling active RhoA mechanoaccumulation during mitosis. Collectively, our data show that RhoA/ROCK and CDK1 not only regulate force generation but also are required for NMIIB to accumulate at the cell cortex in response to compressive forces during mitosis. Interestingly, CDK1 appears to not involve active RhoA to exert its effect on NMIIB mechanoresponse in mitotic cells.

Phosphoregulation of NMIIB tail region is not involved in NMIIB mechanoaccumulation

RhoA/ROCK signaling modulates NMII through phosphorylation of MRLC that associates with NMII's head domain. In addition, NMII is also regulated by the phosphorylation of its tail region, which is involved in regulating myosin II filament assembly.[36] Phosphorylation of NMIIB S1935 lowers the ability of NMIIB to assemble into myofilaments (Figure 4A).[22,25] To study the role of NMIIB tail phosphorylation, we first generated three cell lines stably expressing wild type NMIIB, NMIIB containing a non-phosphorylatable alanine residue at S1935 (S1935A), and NMIIB containing a phosphomimetic aspartate residue at S1935 (S1935D), respectively. The endogenous NMIIB in these cell lines was depleted using CRISPR interference (CRISPRi) that switches off gene expression from its promoter and does not interfere with the transgene expression (Figures S5A–S5C). Cells expressing NMIIB-S1935D showed a decrease in the cytoskeletal fraction compared
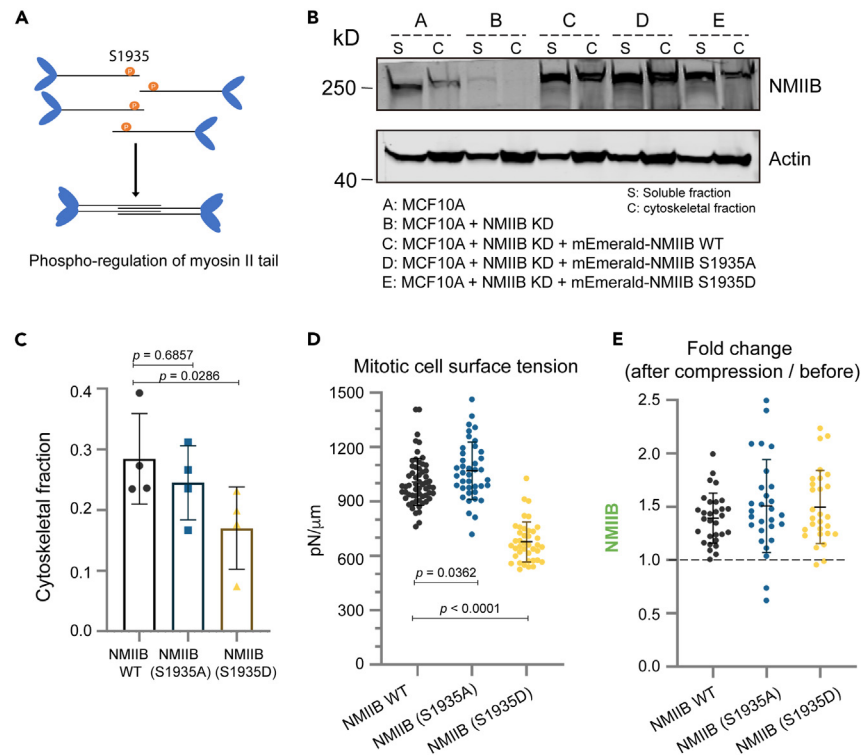
Figure 4. Perturbation of the NMIIB tail domain regulation affects maintenance of the mitotic cell surface tension but less on the NMIIB mechanoresponse

(A) A schematic representation of the phosphoregulation of the NMIIB tail region in controlling the myosin II filament assembly.

(B) A protein blot shows the cytoskeletal fractions and soluble fractions of NMIIB and actin in MCF10A cells expressing different phosphomutants in the absence of endogenous NMIIB. KD, knockdown.

(C) Quantification of the cytoskeletal fractions of NMIIB wild type or phosphomutants from the protein blot.

(D) Measurement of the mitotic cell surface tension by MPA in cells expressing NMIIB (WT), NMIIB (S1935A), or NMIIB (S1935D). NMIIB (WT), 59 cells; NMIIB (S1935A), 40 cells; NMIIB(S1935D), 40 cells.

(E) Quantification of the changes of NMIIB (WT), NMIIB (S1935A), and NMIIB (S1935D) at the cell cortex before and after compression. The fold change is a ratio of the mean intensity after compression to the mean intensity before compression. The dotted indicates ratio of 1 in which a ratio higher than 1 means a positive mechanoresponse. NMIIB (WT), 30 cells; NMIIB (S1935A), 28 cells; NMIIB (S1935D), 28 cells. Data represent means ± SD. Data were collected from 3 independent experiments except for (C) (4 independent experiments). Scale bar, 5 μm. See also Figure S5.

to cells expressing wild type NMIIB or NMIIB-S1935A, indicating less cytoskeletal-bound NMIIB myofilaments were present (Figures 4B and 4C).

When we examined the NMIIB tail phosphomutants, we found that mitotic cells expressing NMIIB-S1935D generated lower cell surface tension (1007.94 ± 130.21 pN/μm in wild type NMIIB and 677.67 ± 111.03 pN/μm in NMIIB S1935D) but were able to demonstrate mechanoaccumulation of NMIIB S1935D after compression (Figures 4D, 4E, and S5D). Mitotic cells expressing NMIIB-S1935A exhibited a similar level of cell surface tension (1069.76 ± 158.13 pN/μm in NMIIB S1935A) and mechanoaccumulation as in cells expressing wild type NMIIB (Figures 4D, 4E, and S5D). Thus, phosphorylation of NMIIB-S1935 at the tail domain affected NMIIB's function in cell surface tension generation but less on the mechanoresponse of NMIIB, in line with the previous study showing that the NMIIB tail domain fine-tuned the NMIIB mechanosensitive dynamics and the phosphomutants could accumulate with varying degree at the cell cortex in epithelial cells in response to mechanical stress.[25]

NMIIB translocation activity is required for its mechanoaccumulation under compression

Our results showed that regulation of NMII's head domain is important for NMIIB to accumulate at the cell cortex in response to compressive forces during mitosis. NMII's head domain has two properties namely actin-binding functions and motor activity to translocate actin filaments.[19] Previous studies showed that NMII's mutations that selectively uncouple these two properties have revealed distinct contributions of each property to NMII's cellular functions.[37–39] To see the roles of these properties in regulating NMIIB mechanoaccumulation, we expressed two previously characterized NMIIB mutants NMIIB-R709C or NMIIB-R241A that are defective in motor activity but retaining their differential ability to bind actin filaments[40,41] (Figure 5A). NMIIB-R709C has higher affinity to actin filaments and hence binds tightly to actin filaments. NMIIB-R241A retains actin binding functions but with a slightly weaker binding affinity to actin filaments as compared to wild type

NMIIB. Both NMIIB-R709C and NMIIB-R241A are defective in translocating actin filaments and have a higher tendency to retain at the cell cortex with differential levels. At steady state, the cortical levels are increased for NMIIB-R709C and decreased for NMIIB-R241A (Figures S6 and S7A; see below). We also expressed one NMIIB mutant K647A that has a weakening actin-binding function[42] in the reporter cells (Figure 5A). We further depleted the endogenous NMIIB in these cell lines using CRISPRi.

Cytoskeletal fractionation analyses showed that cells expressing NMIIB-R709C or R241A have an increased NMIIB cytoskeletal fraction than cells expressing wild type NMIIB or NMIIB-S1935D, indicating a strong cytoskeletal binding of these two NMIIB mutant proteins despite a defective motor activity (Figures 5B and 5C, right panels). Analyses of the dynamics of these two NMIIB mutants at the cell cortex using FRAP has revealed a slow turnover of NMIIB-R709C and NMIIB-R241A at the mitotic cortex (Figures S7B and S7C). To test the ability of these NMIIB mutants to respond to compressive stress in the same cells, we compressed the mitotic cells expressing NMIIB-R709C or R241A. Interestingly, there was no significant increase of cortical NMIIB intensity compared to that of in control cells expressing wild type NMIIB (Figures 5B and 5C, left and middle panels; Figures S6A, S6C, and S6D). In contrast, compression of mitotic cells expressing NMIIB-K647A, which has more NMIIB mutant proteins in the soluble fraction, showed a similar mechanoaccumulation of NMIIB at the cell cortex as in control cells (Figures 5D and S6B). Thus, our data show that the translocation activity of NMIIB, but not just the actin-binding function of the NMIIB's head domain, is required for NMIIB to accumulate at the cell cortex in response to compressive forces during mitosis.

Next, we measured the cell height changes in cells expressing NMIIB-R709C upon compression to see if NMIIB-R709C-expressing mitotic cells would be weaker in sustaining cell geometry in response to compression. In the absence of compression, we observed that mitotic cells expressing NMIIB-R709C has a cell height of 18.89 ± 2.89 μm (n = 57 cells), which is lower than control cell height of 20.24 ± 1.93 μm (n = 48 cells), suggesting that expression of NMIIB-R709C has affected the ability of mitotic cells to round up. Upon compression, mitotic cells expressing NMIIB-R709C reduced its cell height more than control cells (9.91 ± 1.53 μm for NMIIB R709C vs. 11.36 ± 1.37 μm for control), suggesting that cells expressing NMIIB R709C were weaker to withstand the compressive stress. Of note, the cell height measurements performed might be an underestimation as NMIIA was expressed in cells to compensate for the loss of function of NMIIB.

NMIIB translocation activity has a dominant role in regulating its mechanoaccumulation

Next, we asked whether the NMIIB tail mutation S1935D could reduce the tight cytoskeletal association of the NMIIB translocation mutants and hence reverting NMIIB mechanoresponse. To this end, we constructed three NMIIB mutants containing double mutations R709C S1935D, R241A S1935D and K647A S1935D, respectively. We first determined the proportion of the cytoskeletal fraction in protein lysates extracted from these NMIIB double mutants. The results showed that cells expressing NMIIB-R709C S1935D and NMIIB-R241A S1935D have more insoluble cytoskeletal-bound NMIIB mutant proteins compared to control cells (Figure 6A). Compression of these two NMIIB mutant cells showed no significant increase of the cortical NMIIB at the cell cortex compared to cells expressing wild type NMIIB or NMIIB-S1935D (Figures 6B and 6C). Cells expressing NMIIB-K647A S1945D, have more mutant proteins in the soluble fraction compared to control cells and retain the ability to accumulate the cortical NMIIB double mutant protein at the cell cortex in response to compression (Figures 6A–6C). Our data show that NMIIB S1935D mutation does not revert mechanoaccumulation defects of NMIIB translocation mutants, and the NMIIB translocation activity at its head domain plays a dominating role in regulating NMIIB mechanoaccumulation at the cell cortex during mitosis.

DISCUSSION

NMIIs accumulate at the subcellular region with applied mechanical stresses.[23] Mechanoresponse of NMIIs facilitates cellular mechanosensing during cell migration and cell division and confers mechanical adaptation to cancer cells living in physically challenging microenvironment.[43] Within a tissue environment, cells constantly experience mechanical stresses such as compressive stress from surrounding cells and the extracellular matrix. This is particularly significant in an overgrowth tumor environment where solid stress or compressive stress accumulates inside the tumors.[44] Normal or cancer cells that are not able to mechanically adapt to the constantly changing microenvironment by engaging mechanoresponse accumulate cell division defects that lead to aneuploidy.[11,18] A recent study showed that NMIIs are essential for cells to divide under compression to prevent loss of chromosomes and solid human tumors manifest the confinement-signature of NMII suppression.[45]

During the cross-bridge cycle of force generation, NMII binds and slides actin filaments.[19] Interestingly, these two closely related biophysical properties can be genetically uncoupled in different cellular functions of NMIIs. Previous studies showed that maturation of nascent adhesions in migrating cells and division of certain cell types require NMIIs to bind and crosslink actin networks but does not involve its motor activity.[37,39] In contrast, NMIIs bind and slide actin filaments during cell-cell adhesions and embryonic cell division.[38,40,46] We tested this differential requirement of NMII in its mechanoresponse during mitosis. Using two NMIIB mutations (R709C and R241A in NMIIB) that are motor dead but retaining actin-binding function,[37,40] we revealed that mechanoaccumulation of NMIIB at the mitotic cell cortex requires the translocation activity of NMIIB. Interestingly, a mutation in loop 2 of the actin-binding surface of NMIIB (K647A in NMIIB), which regulates the cleft closure of U50 and L50 subdomains of NMIIs for strong actin-binding function,[42,47] does not dampen NMIIB mechanoresponse. Thus, actin-binding function of NMIIs alone is not sufficient to regulate mechanoaccumulation of NMIIB at the mitotic cell cortex, and counterintuitively, the motor activity of NMIIB in driving actin filament translocation is essential in NMIIB mechanoresponse. Interestingly, motor activity is required to control penetration of myosin II into the otherwise sterically limited actin cortex.[48] It is possible that the motor dead NMIIB mutants could not efficiently penetrate the actin cortex in response to compression to accumulate at the cortex. The slow turnover of NMIIB-R709C and
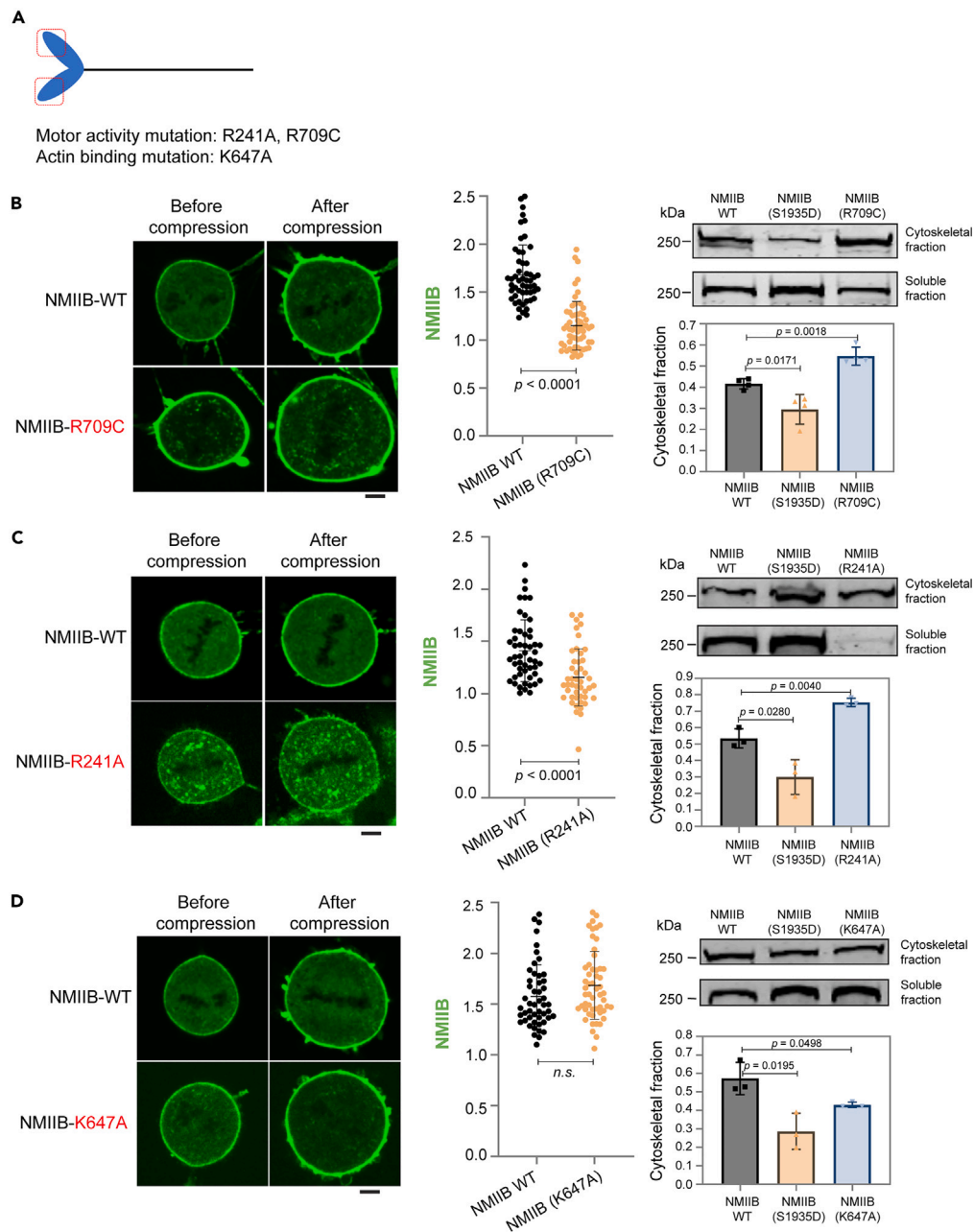
Figure 5. NMIIB that is motor-dead but retaining actin-binding function is defective in mechanoaccumulation

(A) A diagram showing the motor activity mutations and actin-binding mutations of NMIIB used in the study.

(B) Left panel, micrographs of a cell expressing NMIIB-WT and a cell expressing NMIIB-R709C before and after compression; middle panel, the fold change is a ratio of the mean intensity after compression to the mean intensity before compression. A ratio higher than 1 means a positive mechanoresponse. NMIIB-WT, 53 cells; NMIIB-R709C, 60 cells; right panel, a protein blot and quantification of the cytoskeletal fractions and soluble fractions of NMIIB wild type and NMIIB-R709C mutant proteins.

(C) Left panel, micrographs of a cell expressing NMIIB-WT and a cell expressing NMIIB-R241A before and after compression; middle panel, the fold change is a ratio of the mean intensity after compression to the mean intensity before compression. A ratio higher than 1 means a positive mechanoresponse. NMIIB-WT, 51 cells; NMIIB-R241A, 46 cells; right panel, a protein blot and quantification of the cytoskeletal fractions and soluble fractions of NMIIB wild type and NMIIB-R241A mutant proteins.

(D) Left panel, micrographs of a cell expressing NMIIB-WT and a cell expressing NMIIB-K647A before and after compression; middle panel, the fold change is a ratio of the mean intensity after compression to the mean intensity before compression. A ratio higher than 1 means a positive mechanoresponse. NMIIB-WT, 50 cells; NMIIB-K647A, 54 cells; right panel, a protein blot and quantification of the cytoskeletal fractions and soluble fractions of NMIIB wild type and NMIIB-K647A mutant proteins. Data represent means ± SD. Data were collected from 3 independent experiments except (B) protein blot (4 independent experiments). Scale bar, 5 μm. See also Figures S6 and S7.
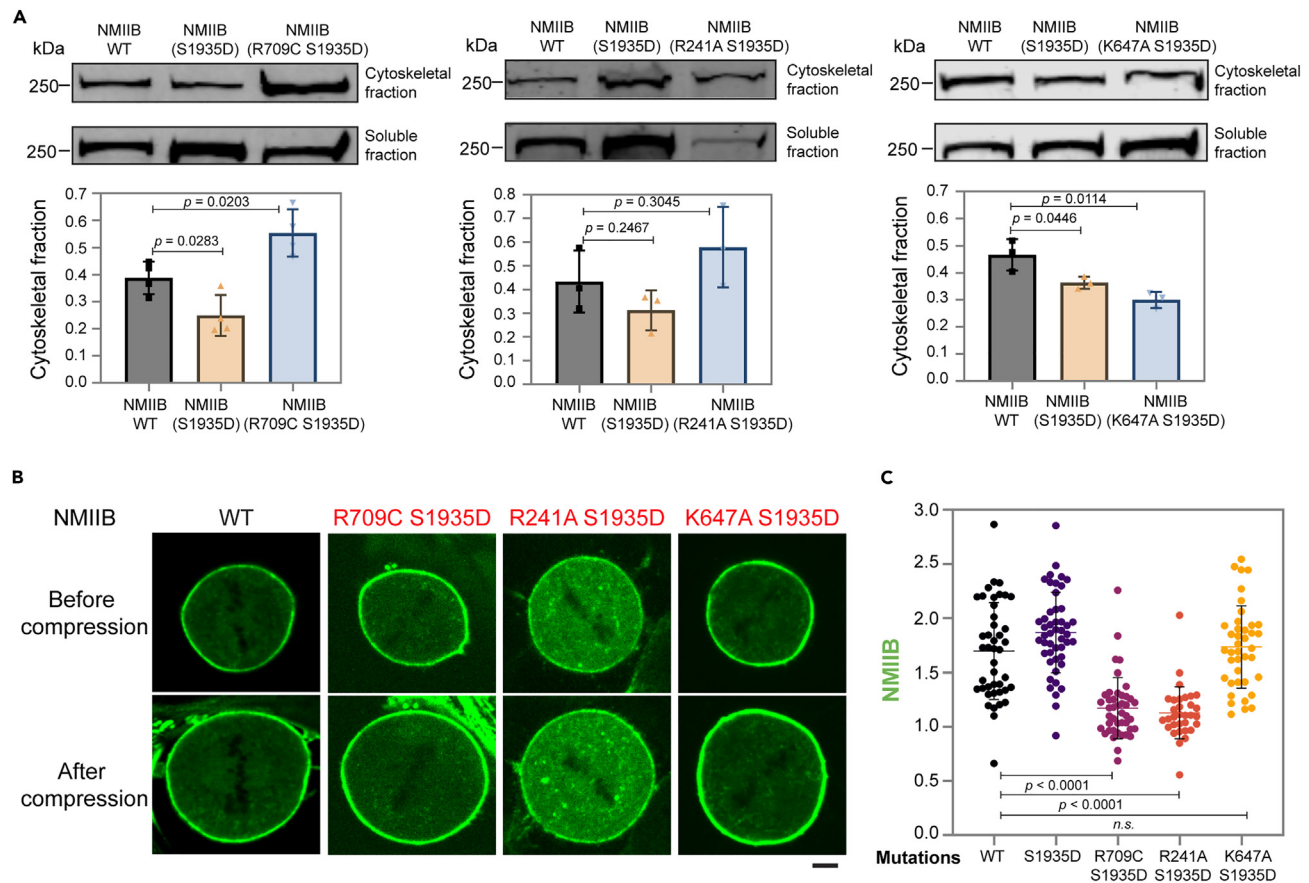
Figure 6. The translocation activity plays a dominant role in regulating NMIIB mechanoaccumulation

(A) Protein blots and quantification of the cytoskeletal fractions and soluble fractions of NMIIB wild type and NMIIB double mutant proteins.

(B) Micrographs of cells expressing wild type NMIIB or NMIIB double mutants before and after compression.

(C) The fold change is a ratio of the mean intensity after compression to the mean intensity before compression. A ratio higher than 1 means a positive mechanoresponse. NMIIB-WT, 43 cells; NMIIB-S1935D, 48 cells; NMIIB-R709C S1935D, 43 cells; NMIIB-R241A S1935D, 32 cells; NMIIB-K647A S1935D, 40 cells. Data represent means ± SD. Data were collected from 3 independent experiments except (A) left panel (4 independent experiments). Scale bar, 5 μm.

NMIIB-R241A at the cell cortex and differential cortical localizations are consistent with this notion and may contribute to defective mechanoaccumulation of NMIIB at the cell cortex in response to compression.

Activation of RhoA/ROCK signaling pathway leads to MRLC phosphorylation and is associated with an increase of the actin-activated ATPase kinetics of myosin head domain and hence its motor activity.[20,36,49] In addition to the role of RhoA/ROCK in force generation to promote mitotic cell rounding, we found that this signaling pathway is involved in mechanoaccumulation of NMIIB during mitosis. Through the effector ROCK, mechanoaccumulation of active RhoA drives higher activation of myosin motor domain and stabilization of NMIIB at the cell cortex in response to compressive forces in mitotic cells. Interestingly, CDK1 inhibition leads to decreased cortical NMIIB but higher cortical active RhoA in compressed mitotic cells. Similar observation has been identified in starfish oocytes undergoing meiotic division in which RhoA is activated when CDK1 is inhibited during surface contraction waves.[50] Thus, during mitosis, CDK1 does not appear to involve RhoA to regulate NMIIB mechanoaccumulation. This contrasts with CDK1's function in activating Ect2/RhoA/ROCK signaling and NMIIs when cells enter mitosis from interphase.[14,17] Our study showed that knockdown of Ect2 did not abolish active RhoA and NMIIB mechanoaccumulation at the cell cortex, suggesting a differential regulation of RhoA and NMIIB by CDK1/Ect2 signaling during mitosis, particularly in mechanoresponse. A genome-scale screening has revealed genes that are involved in regulating mitotic cell mechanics.[51] It is possible that some of the genes identified in the screening are involved in regulating NMIIB mechanoresponse during mitosis without RhoA involvement. Future studies will address the involvement of these genes in CDK1/RhoA regulation. The roles of RhoA/ROCK and CDK1 during mitosis in regulating force generation and cell rounding are well established. However, our study offers a systematic analysis of RhoA/ROCK and CDK1 in regulating force generation (cell surface tension) and NMIIB mechanoresponse of the same single mitotic cells without chemically arresting cells at mitosis, which could be a reference for future studies involving cell mechanics during mitosis.

Mechanical activation of RhoA happens in interphase cells particularly at the cell-cell adherens junctions and the cell-matrix focal adhesion to reinforce actomyosin contractility in response to mechanical stress.[26,29,52] Mechanoaccumulation of active RhoA at the cell cortex during

mitosis was not previously identified although inhibition of its downstream effector ROCK led to a decreased mechanoresponse of NMII.[24] In our study, we employed widely used live-cell active RhoA reporters[35,53] and focused only on mitotic cells using a microscopy with confocality and high temporal resolution. This has facilitated a sensitive detection of RhoA mechanoresponse at the cell cortex when mitosis is mechanically challenged. Furthermore, we have observed the mechanoresponse of active RhoA and NMIIB in rounded interphase cells, which has been shown previously in compressed cells cultured in 3D matrixes.[26] It will be interesting to see mechanistically whether and how mitotic cells and interphase cells are different in responding to compressive stress. The nucleus and the nuclear membrane function as mechanosensors in interphase cells to respond to compression.[54,55] These cellular structures, however, break down during mitosis. Thus, it is possible that the cell cortex has a more direct role in mechanosensing in response to compression during mitosis.

Our finding implies that NMII mechanoaccumulation involves lever arm movement generated by the motor activity. Lever arm movement is coupled to nucleotide state changes during Pi release and ADP release and generates NMIIs of different nucleotide states and actin-binding affinity.[19,56–58] Consistently, NMIIs engineered to have longer neck structure and hence larger lever arm movement have stronger ability to mechanoaccumulate in cells.[23] We propose a model that NMIIB species of different actin-binding affinity are generated after lever arm movement and nucleotide state changes. These NMIIB species bind actin filaments at varying affinity and in ensemble display accumulation in response to compressive forces during mitosis. This notion is supported by the existence of "Goldilocks zone" for the actin-binding affinity for an optimal mechanoaccumulation as described for actin-binding proteins such as α-actinin, filamin and NMIIs.[24]

Limitations of the study

In our study, we performed mechanical compression and analyses on single cells in isolation. It will be important in future to examine the mechanoresponse of NMIIs and active RhoA in a more physiological 3D environment such as one that is confined by neighboring cells. In addition, our findings of mechanosensitive accumulation of active RhoA at the cell cortex requires more studies to understand its mechanisms of mechanical activation and mechanistic differences in cells during interphase and mitosis.

STAR★METHODS

Detailed methods are provided in the online version of this paper and include the following:

- KEY RESOURCES TABLE
- RESOURCE AVAILABILITY
  - Lead contact
  - Materials availability
  - Data and code availability
- EXPERIMENTAL MODELS AND STUDY PARTICIPANTS DETAILS
  - Cell lines
- METHOD DETAILS
  - Drug treatments
  - Lentiviral expression constructs
  - Mitotic cell preparation
  - Elastic polyacrylamide gel preparation
  - Micropipette aspiration (MPA)
  - Spinning-disk confocal microscopy for live-cell imaging
  - Mitotic cell compression and live-cell imaging
  - Interphase cell compression
  - Image analysis and processing
  - FRAP
  - Cytoskeletal fractionation
  - Protein immunoblotting
  - Quantitative real-time PCR (qPCR) for checking endogenous NMIIB
- QUANTIFICATION AND STATISTICAL ANALYSIS

SUPPLEMENTAL INFORMATION

Supplemental information can be found online at https://doi.org/10.1016/j.isci.2023.107773.

AUTHOR CONTRIBUTIONS

C.W. and J.D. designed, performed experiments, and analyzed data. S.D. prepared elastic gels used in the study. Q.W. and X.G. provided the devices and technical expertise for micropipette aspiration. T.G.C. conceived the study, designed experiments, supervised the study, and prepared the manuscript with inputs from all authors.

DECLARATION OF INTERESTS

The authors declare no competing interests.

INCLUSION AND DIVERSITY

We support inclusive, diverse, and equitable conduct of research.

REFERENCES

1. Murrell, M., Oakes, P.W., Lenz, M., and Gardel, M.L. (2015). Forcing cells into shape: the mechanics of actomyosin contractility. Nat. Rev. Mol. Cell Biol. 16, 486–498. https://doi.org/10.1038/nrm4012.

2. Vicente-Manzanares, M., Ma, X., Adelstein, R.S., and Horwitz, A.R. (2009). Non-muscle myosin II takes centre stage in cell adhesion and migration. Nat. Rev. Mol. Cell Biol. 10, 778–790. https://doi.org/10.1038/nrm2786.

3. Kelkar, M., Bohec, P., and Charras, G. (2020). Mechanics of the cellular actin cortex: From signalling to shape change. Curr. Opin. Cell Biol. 66, 69–78. https://doi.org/10.1016/j.ceb.2020.05.008.

4. Fischer-Friedrich, E., Toyoda, Y., Cattin, C.J., Müller, D.J., Hyman, A.A., and Jülicher, F. (2016). Rheology of the Active Cell Cortex in Mitosis. Biophys. J. 111, 589–600. https://doi.org/10.1016/j.bpj.2016.06.008.

5. Chugh, P., Clark, A.G., Smith, M.B., Cassani, D.A.D., Dierkes, K., Ragab, A., Roux, P.P., Charras, G., Salbreux, G., and Paluch, E.K. (2017). Actin cortex architecture regulates cell surface tension. Nat. Cell Biol. 19, 689–697. https://doi.org/10.1038/ncb3525.

6. Fischer-Friedrich, E., Hyman, A.A., Jülicher, F., Müller, D.J., and Helenius, J. (2014). Quantification of surface tension and internal pressure generated by single mitotic cells. Sci. Rep. 4, 6213. https://doi.org/10.1038/srep06213.

7. Stewart, M.P., Helenius, J., Toyoda, Y., Ramanathan, S.P., Muller, D.J., and Hyman, A.A. (2011). Hydrostatic pressure and the actomyosin cortex drive mitotic cell rounding. Nature 469, 226–230. https://doi.org/10.1038/nature09642.

8. Ramkumar, N., and Baum, B. (2016). Coupling changes in cell shape to chromosome segregation. Nat. Rev. Mol. Cell Biol. 17, 511–521. https://doi.org/10.1038/nrm.2016.75.

9. Ramanathan, S.P., Helenius, J., Stewart, M.P., Cattin, C.J., Hyman, A.A., and Muller, D.J. (2015). Cdk1-dependent mitotic enrichment of cortical myosin II promotes cell rounding against confinement. Nat. Cell Biol. 17, 148–159. https://doi.org/10.1038/ncb3098.

10. Nishimura, K., Johmura, Y., Deguchi, K., Jiang, Z., Uchida, K.S.K., Suzuki, N., Shimada, M., Chiba, Y., Hirota, T., Yoshimura, S.H., et al. (2019). Cdk1-mediated DIAPH1 phosphorylation maintains metaphase cortical tension and inactivates the spindle assembly checkpoint at anaphase. Nat. Commun. 10, 981. https://doi.org/10.1038/s41467-019-08957-w.

11. Matthews, H.K., Ganguli, S., Plak, K., Taubenberger, A.V., Win, Z., Williamson, M., Piel, M., Guck, J., and Baum, B. (2020). Oncogenic Signaling Alters Cell Shape and Mechanics to Facilitate Cell Division under Confinement. Dev. Cell 52, 563–573.e3. https://doi.org/10.1016/j.devcel.2020.01.004.

12. Lancaster, O.M., Le Berre, M., Dimitracopoulos, A., Bonazzi, D., Zlotek-Zlotkiewicz, E., Picone, R., Duke, T., Piel, M., and Baum, B. (2013). Mitotic rounding alters cell geometry to ensure efficient bipolar spindle formation. Dev. Cell 25, 270–283. https://doi.org/10.1016/j.devcel.2013.03.014.

13. Cadart, C., Zlotek-Zlotkiewicz, E., Le Berre, M., Piel, M., and Matthews, H.K. (2014). Exploring the function of cell shape and size during mitosis. Dev. Cell 29, 159–169. https://doi.org/10.1016/j.devcel.2014.04.009.

14. Matthews, H.K., Delabre, U., Rohn, J.L., Guck, J., Kunda, P., and Baum, B. (2012). Changes in Ect2 localization couple actomyosin-dependent cell shape changes to mitotic progression. Dev. Cell 23, 371–383. https://doi.org/10.1016/j.devcel.2012.06.003.

15. Maddox, A.S., and Burridge, K. (2003). RhoA is required for cortical retraction and rigidity during mitotic cell rounding. J. Cell Biol. 160, 255–265. https://doi.org/10.1083/jcb.200207130.

16. Chew, T.G., Huang, J., Palani, S., Sommese, R., Kamnev, A., Hatano, T., Gu, Y., Oliferenko, S., Sivaramakrishnan, S., and Balasubramanian, M.K. (2017). Actin turnover maintains actin filament homeostasis during cytokinetic ring contraction. J. Cell Biol. 216, 2657–2667. https://doi.org/10.1083/jcb.201701104.

17. Rosa, A., Vlassaks, E., Pichaud, F., and Baum, B. (2015). Ect2/Pbl acts via Rho and polarity proteins to direct the assembly of an isotropic actomyosin cortex upon mitotic entry. Dev. Cell 32, 604–616. https://doi.org/10.1016/j.devcel.2015.01.012.

18. Cattin, C.J., Düggelin, M., Martinez-Martin, D., Gerber, C., Müller, D.J., and Stewart, M.P. (2015). Mechanical control of mitotic progression in single animal cells. Proc. Natl. Acad. Sci. USA 112, 11258–11263. https://doi.org/10.1073/pnas.1502029112.

19. Sweeney, H.L., and Houdusse, A. (2010). Structural and functional insights into the Myosin motor mechanism. Annu. Rev. Biophys. 39, 539–557. https://doi.org/10.1146/annurev.biophys.050708.133751.

20. Amano, M., Ito, M., Kimura, K., Fukata, Y., Chihara, K., Nakano, T., Matsuura, Y., and Kaibuchi, K. (1996). Phosphorylation and activation of myosin by Rho-associated kinase (Rho-kinase). J. Biol. Chem. 271, 20246–20249. https://doi.org/10.1074/jbc.271.34.20246.

21. Garrido-Casado, M., Asensio-Juárez, G., and Vicente-Manzanares, M. (2021). Nonmuscle Myosin II Regulation Directs Its Multiple Roles in Cell Migration and Division. Annu. Rev. Cell Dev. Biol. 37, 285–310. https://doi.org/10.1146/annurev-cellbio-042721-105528.

22. Juanes-Garcia, A., Chapman, J.R., Aguilar-Cuenca, R., Delgado-Arevalo, C., Hodges, J., Whitmore, L.A., Shabanowitz, J., Hunt, D.F., Horwitz, A.R., and Vicente-Manzanares, M. (2015). A regulatory motif in nonmuscle myosin II-B regulates its role in migratory front-back polarity. J. Cell Biol. 209, 23–32. https://doi.org/10.1083/jcb.201407059.

23. Luo, T., Mohan, K., Iglesias, P.A., and Robinson, D.N. (2013). Molecular mechanisms of cellular mechanosensing. Nat. Mater. 12, 1064–1071. https://doi.org/10.1038/nmat3772.

24. Schiffhauer, E.S., Luo, T., Mohan, K., Srivastava, V., Qian, X., Griffis, E.R., Iglesias, P.A., and Robinson, D.N. (2016).

Mechanoaccumulative Elements of the Mammalian Actin Cytoskeleton. Curr. Biol. *26*, 1473–1479. https://doi.org/10.1016/j.cub.2016.04.007.

25. Schiffhauer, E.S., Ren, Y., Iglesias, V.A., Kothari, P., Iglesias, P.A., and Robinson, D.N. (2019). Myosin IIB assembly state determines its mechanosensitive dynamics. J. Cell Biol. *218*, 895–908. https://doi.org/10.1083/jcb.201806058.

26. Boyle, S.T., Kular, J., Nobis, M., Ruszkiewicz, A., Timpson, P., and Samuel, M.S. (2020). Acute compressive stress activates RHO/ROCK-mediated cellular processes. Small GTPases *11*, 354–370. https://doi.org/10.1080/21541248.2017.1413496.

27. Priya, R., Gomez, G.A., Budnar, S., Verma, S., Cox, H.L., Hamilton, N.A., and Yap, A.S. (2015). Feedback regulation through myosin II confers robustness on RhoA signalling at E-cadherin junctions. Nat. Cell Biol. *17*, 1282–1293. https://doi.org/10.1038/ncb3239.

28. Piekny, A.J., and Glotzer, M. (2008). Anillin is a scaffold protein that links RhoA, actin, and myosin during cytokinesis. Curr. Biol. *18*, 30–36. https://doi.org/10.1016/j.cub.2007.11.068.

29. Acharya, B.R., Nestor-Bergmann, A., Liang, X., Gupta, S., Duszyc, K., Gauquelin, E., Gomez, G.A., Budnar, S., Marcq, P., Jensen, O.E., et al. (2018). A Mechanosensitive RhoA Pathway that Protects Epithelia against Acute Tensile Stress. Dev. Cell *47*, 439–452.e6. https://doi.org/10.1016/j.devcel.2018.09.016.

30. Cavanaugh, K.E., Staddon, M.F., Chmiel, T.A., Harmon, R., Budnar, S., Yap, A.S., Banerjee, S., and Gardel, M.L. (2022). Force-dependent intercellular adhesion strengthening underlies asymmetric adherens junction contraction. Curr. Biol. *32*, 1986–2000.e5. https://doi.org/10.1016/j.cub.2022.03.024.

31. Beaudet, D., Pham, N., Skaik, N., and Piekny, A. (2020). Importin binding mediates the intramolecular regulation of anillin during cytokinesis. Mol. Biol. Cell *31*, 1124–1139. https://doi.org/10.1091/mbc.E20-01-0006.

32. Taneja, N., Bersi, M.R., Baillargeon, S.M., Fenix, A.M., Cooper, J.A., Ohi, R., Gama, V., Merryman, W.D., and Burnette, D.T. (2020). Precise Tuning of Cortical Contractility Regulates Cell Shape during Cytokinesis. Cell Rep. *31*, 107477. https://doi.org/10.1016/j.celrep.2020.03.041.

33. Képiró, M., Várkuti, B.H., Végner, L., Vörös, G., Hegyi, G., Varga, M., and Málnási-Csizmadia, A. (2014). para-Nitroblebbistatin, the non-cytotoxic and photostable myosin II inhibitor. Angew. Chem., Int. Ed. Engl. *53*, 8211–8215. https://doi.org/10.1002/anie.201403540.

34. Rauscher, A.Á., Gyimesi, M., Kovács, M., and Málnási-Csizmadia, A. (2018). Targeting Myosin by Blebbistatin Derivatives: Optimization and Pharmacological Potential. Trends Biochem. Sci. *43*, 700–713. https://doi.org/10.1016/j.tibs.2018.06.006.

35. Mahlandt, E.K., Arts, J.J.G., van der Meer, W.J., van der Linden, F.H., Tol, S., van Buul, J.D., Gadella, T.W.J., and Goedhart, J. (2021). Visualizing endogenous Rho activity with an improved localization-based, genetically encoded biosensor. J. Cell Sci. *134*, jcs258823. https://doi.org/10.1242/jcs.258823.

36. Heissler, S.M., and Sellers, J.R. (2016). Various Themes of Myosin Regulation. J. Mol. Biol.

428, 1927–1946. https://doi.org/10.1016/j.jmb.2016.01.022.

37. Ma, X., Kovács, M., Conti, M.A., Wang, A., Zhang, Y., Sellers, J.R., and Adelstein, R.S. (2012). Nonmuscle myosin II exerts tension but does not translocate actin in vertebrate cytokinesis. Proc. Natl. Acad. Sci. USA *109*, 4509–4514. https://doi.org/10.1073/pnas.1116268109.

38. Smutny, M., Cox, H.L., Leerberg, J.M., Kovacs, E.M., Conti, M.A., Ferguson, C., Hamilton, N.A., Parton, R.G., Adelstein, R.S., and Yap, A.S. (2010). Myosin II isoforms identify distinct functional modules that support integrity of the epithelial zonula adherens. Nat. Cell Biol. *12*, 696–702. https://doi.org/10.1038/ncb2072.

39. Choi, C.K., Vicente-Manzanares, M., Zareno, J., Whitmore, L.A., Mogilner, A., and Horwitz, A.R. (2008). Actin and alpha-actinin orchestrate the assembly and maturation of nascent adhesions in a myosin II motor-independent manner. Nat. Cell Biol. *10*, 1039–1050. https://doi.org/10.1038/ncb1763.

40. Osório, D.S., Chan, F.Y., Saramago, J., Leite, J., Silva, A.M., Sobral, A.F., Gassmann, R., and Carvalho, A.X. (2019). Crosslinking activity of non-muscle myosin II is not sufficient for embryonic cytokinesis in C. elegans. Development *146*, dev179150. https://doi.org/10.1242/dev.179150.

41. Kim, K.Y., Kovács, M., Kawamoto, S., Sellers, J.R., and Adelstein, R.S. (2005). Disease-associated mutations and alternative splicing alter the enzymatic and motile activity of nonmuscle myosins II-B and II-C. J. Biol. Chem. *280*, 22769–22775. https://doi.org/10.1074/jbc.M503488200.

42. von der Ecken, J., Heissler, S.M., Pathan-Chhatbar, S., Manstein, D.J., and Raunser, S. (2016). Cryo-EM structure of a human cytoplasmic actomyosin complex at near-atomic resolution. Nature *534*, 724–728. https://doi.org/10.1038/nature18295.

43. Nguyen, L.T.S., Jacob, M.A.C., Parajón, E., and Robinson, D.N. (2022). Cancer as a biophysical disease: Targeting the mechanical-adaptability program. Biophys. J. *121*, 3573–3585. https://doi.org/10.1016/j.bpj.2022.04.039.

44. Nia, H.T., Munn, L.L., and Jain, R.K. (2020). Physical traits of cancer. Science *370*, eaaz0868. https://doi.org/10.1126/science.aaz0868.

45. Brandon, H., Hayes, P.K.Z., Wang, M., Pfeifer, C.R., Xia, Y., Phan, S., Andrechak, J.C., Du, J., Tobin, M.P., Anlas, A., Lawrence, D., et al. (2023). Confinement with Myosin-II Suppression Increases Heritable Loss of Chromosomes, Using Live-Cell ChReporters. Preprint at BioRxiv. https://www.biorxiv.org/content/10.1101/2023.02.25.530049v1.

46. Kasza, K.E., Supriyatno, S., and Zallen, J.A. (2019). Cellular defects resulting from disease-related myosin II mutations in Drosophila. Proc. Natl. Acad. Sci. USA *116*, 22205–22211. https://doi.org/10.1073/pnas.1909227116.

47. Onishi, H., Mikhailenko, S.V., and Morales, M.F. (2006). Toward understanding actin activation of myosin ATPase: the role of myosin surface loops. Proc. Natl. Acad. Sci. USA *103*, 6136–6141. https://doi.org/10.1073/pnas.0601595103.

48. Truong Quang, B.A., Peters, R., Cassani, D.A.D., Chugh, P., Clark, A.G., Agnew, M., Charras, G., and Paluch, E.K. (2021). Extent of

myosin penetration within the actin cortex regulates cell surface mechanics. Nat. Commun. *12*, 6511. https://doi.org/10.1038/s41467-021-26611-2.

49. Nayak, A., Wang, T., Franz, P., Steffen, W., Chizhov, I., Tsiavaliaris, G., and Amrute-Nayak, M. (2020). Single-molecule analysis reveals that regulatory light chains fine-tune skeletal myosin II function. J. Biol. Chem. *295*, 7046–7059. https://doi.org/10.1074/jbc.RA120.012774.

50. Bischof, J., Brand, C.A., Somogyi, K., Májer, I., Thome, S., Mori, M., Schwarz, U.S., and Lénárt, P. (2017). A cdk1 gradient guides surface contraction waves in oocytes. Nat. Commun. *8*, 849. https://doi.org/10.1038/s41467-017-00979-6.

51. Toyoda, Y., Cattin, C.J., Stewart, M.P., Poser, I., Theis, M., Kurzchalia, T.V., Buchholz, F., Hyman, A.A., and Müller, D.J. (2017). Genome-scale single-cell mechanical phenotyping reveals disease-related genes involved in mitotic rounding. Nat. Commun. *8*, 1266. https://doi.org/10.1038/s41467-017-01147-6.

52. Guilluy, C., Swaminathan, V., Garcia-Mata, R., O'Brien, E.T., Superfine, R., and Burridge, K. (2011). The Rho GEFs LARG and GEF-H1 regulate the mechanical response to force on integrins. Nat. Cell Biol. *13*, 722–727. https://doi.org/10.1038/ncb2254.

53. Koh, S.P., Pham, N.P., and Piekny, A. (2022). Seeing is believing: tools to study the role of Rho GTPases during cytokinesis. Small GTPases *13*, 211–224. https://doi.org/10.1080/21541248.2021.1957384.

54. Lomakin, A.J., Cattin, C.J., Cuvelier, D., Alraies, Z., Molina, M., Nader, G.P.F., Srivastava, N., Sáez, P.J., Garcia-Arcos, J.M., Zhitnyak, I.Y., et al. (2020). The nucleus acts as a ruler tailoring cell responses to spatial constraints. Science *370*, eaba2894. https://doi.org/10.1126/science.aba2894.

55. Venturini, V., Pezzano, F., Català Castro, F., Häkkinen, H.M., Jiménez-Delgado, S., Colomer-Rosell, M., Marro, M., Tolosa-Ramon, Q., Paz-López, S., Valverde, M.A., et al. (2020). The nucleus measures shape changes for cellular proprioception to control dynamic cell behavior. Science *370*, eaba2644. https://doi.org/10.1126/science.aba2644.

56. Trivedi, D.V., Muretta, J.M., Swenson, A.M., Davis, J.P., Thomas, D.D., and Yengo, C.M. (2015). Direct measurements of the coordination of lever arm swing and the catalytic cycle in myosin V. Proc. Natl. Acad. Sci. USA *112*, 14593–14598. https://doi.org/10.1073/pnas.1517566112.

57. Debold, E.P. (2021). Recent insights into the relative timing of myosin's powerstroke and release of phosphate. Cytoskeleton (Hoboken) *78*, 448–458. https://doi.org/10.1002/cm.21695.

58. Wulf, S.F., Ropars, V., Fujita-Becker, S., Oster, M., Hofhaus, G., Trabuco, L.G., Pylypenko, O., Sweeney, H.L., Houdusse, A.M., and Schröder, R.R. (2016). Force-producing ADP state of myosin bound to actin. Proc. Natl. Acad. Sci. USA *113*, E1844–E1852. https://doi.org/10.1073/pnas.1516598113.

59. Le Berre, M., Zlotek-Zlotkiewicz, E., Bonazzi, D., Lautenschlaeger, F., and Piel, M. (2014). Methods for two-dimensional cell confinement. Methods Cell Biol. *121*, 213–229. https://doi.org/10.1016/B978-0-12-800281-0.00014-2.

STAR★METHODS

KEY RESOURCES TABLE

REAGENT or RESOURCE	SOURCE	IDENTIFIER
Antibodies		
MYH10(NMIIB) antibody	Proteintech	Cat#19673-1-AP RRID:AB_10858231
Beta-actin antibody	Genscipt	Cat#A00702
GFP antibody	HuaBio	Cat#ET1604-26
GAPDH antibody	Cell Signaling Technology	Cat#5174
p-MLC2(ser19) antibody	Cell Signaling Technology	Cat#3675
Alexa Fluor Plus 800-conjugated goat anti-rabbit IgG secondary antibody	Thermo Fisher Scientific	Cat#A32735 RRID:AB_2633284
Alexa Fluor 680-conjugated goat anti-mouse IgG secondary antibody	Thermo Fisher Scientific	Cat#A32729 RRID: AB_2633278
Chemicals, peptides, and recombinant proteins		
p-nitro-blebbistatin	Cayman Chemical	Cat#24171
C3 exoenzyme	Cytoskeleton	Cat#CT04
Y-27632	MedChemExpress	Cat#HY-10583
RO-3306	Selleckchem	Cat#S7747
Binding-silane	Sangon	Cat#C500226
Acrylamide	Sangon	Cat#A501033
Bis-arcylamide	Sangon	Cat#A100172
APS(Ammonium persulfate)	Macklin	Cat#A801034
TEMED	Sangon	Cat#A610508
DMEM F-12	Shanghai BasalMedia	Cat#X098A1
Glutamax	Gibco	Cat#35050061
Horse serum	Biological Industries	Cat#04-124
EGF	Gibco	Cat#PHG0311
Hydrocortisone	MedChemExpress	Cat#HY-N0583
Cholera toxin	Sigma-Aldrich	Cat#C8052
Insulin	Biological Industries	Cat#41-975-100
Pen/Strep	Biological Industries	Cat#03-031-1B
Puromycin dihydrochloride hydrate	Sangon Biotech	Cat#A610593
Blasticidin	Solarbio	Cat#B9300
SiR-DNA	Cytoskeleton	Cat#CY-SC007
PIPES	Sigma-Aldrich	Cat#P6757
Adenosine 5′-triphosphate magnesium salt	Sigma-Aldrich	Cat#A9187
Triton X-100	Sigma-Aldrich	Cat#X100-500ML
Protease inhibitor cocktail	Thermo Fisher Scientific	Cat#11836153001
Poly-L-lysine solution	Beyotime	Cat#C0313
Critical commercial assays		
FastPure Cell/Tissue Total RNA Isolation Kit	Vazyme	Cat#RC101-01
HiScript II Q RT SuperMix	Vazyme	Cat#R223-01
ChamQ Universal SYBR qPCR Master Mix	Vazyme	Cat#Q711-02

Continued

REAGENT or RESOURCE	SOURCE	IDENTIFIER
MycoBlue Mycoplasma Detector	Vazyme	Cat#D101
Experimental models: Cell lines		
MCF-10A cells expressing dTomato-2xrGBD	This paper	N/A
MCF-10A cells expressing mRuby2-AHPH and mEmerald-NMIIB	This paper	N/A
MCF10A cells expressing mEmerald-NMIIB WT	This paper	N/A
MCF10A cells expressing mEmerald-NMIIB S1935A	This paper	N/A
MCF10A cells expressing mEmerald-NMIIB S1935D	This paper	N/A
MCF10A cells expressing mEmerald-NMIIB(R709C)	This paper	N/A
MCF10A cells expressing mEmerald-NMIIB (R709C + S1935D)	This paper	N/A
MCF10A cells expressing mEmerald-NMIIB(R241A)	This paper	N/A
MCF10A cells expressing mEmerald-NMIIB(R241A + S1935D)	This paper	N/A
MCF10A cells expressing mEmerald-NMIIB(K647A)	This paper	N/A
MCF10A cells expressing mEmerald-NMIIB (K647A + S1935D)	This paper	N/A
Oligonucleotides		
qPCR primers for GAPDH For: 5'CAGGAGGCATTGCTGATGAT3' Rev: 5'GAAGGCTGGGGCTCATTT3'	Sangon	Cat#B661104-0001
qPCR primers for NMIIB For: 5'CCTCATGCTGACCTTGCAAA3' Rev: 5'GGACACAAAACCAATATTCCCATT3'	This paper	N/A
qPCR primers for ECT2 For: 5' ACTACTGGGAGGACTAGCTTG3' Rev: 5' CACTCTTGTTTCAATCTGAGGCA3'	This paper	N/A
5'GTGCTAAAGGAGCCCGGCGG3' CRISPRi sgRNA1 for NMIIB	This paper	N/A
5'GCTGGATCTGTGGTCGCGGC3' CRISPRi sgRNA2 for NMIIB	This paper	N/A
5'GCTGGATCTGTGGTCGCGGC3' CRISPRi sgRNA3 for NMIIB	This paper	N/A
5' GGGCCGCCGGCGAGGAATGG3' CRISPRi sgRNA2 for ECT2	This paper	N/A
Recombinant DNA		
pTGL0193-LV007-mEmerald-MyosinIIB	This paper	N/A
pTGL0373-LV007-mEmerald-Myosin IIB (S1935A)	This paper	N/A
pTGL0374-LV007-mEmerald-Myosin IIB (S1935D)	This paper	N/A

Continued

REAGENT or RESOURCE	SOURCE	IDENTIFIER
pTGL0386-Lenti-(BB)-EF1a-KRAB-dCas9-P2A-BlastR	Jorge Ferrer	Addgene plasmid #118154
pTGL0427-pCDH-CMV-mRuby2-AHPH	This paper	N/A
pTGL0582-LV007-mEmerald-Myosin IIB (R241A)	This paper	N/A
pTGL0583-LV007-mEmerald-Myosin IIB (R241A + S1935D)	This paper	N/A
pTGL0584-LV007-mEmerald-Myosin IIB (R709C)	This paper	N/A
pTGL0585-LV007-mEmerald-Myosin IIB (R709C + S1935D)	This paper	N/A
pTGL0589-LV007-mEmerald-Myosin IIB(K647A)	This paper	N/A
pTGL0590-LV007-mEmerald-Myosin IIB(K647A + S1935D)	This paper	N/A
pTGL0594-pCDH-EF1a-MCS dtomato-2xGBD -PGK-Neo	This paper	N/A
pRSV-Rev	Didier Trono	Addgene plasmid #12253
pMDLg/pRRE	Didier Trono	Addgene plasmid #12251
pMD2.G	Didier Trono	Addgene plasmid #12259
pCRISPRi0003- Lenti-(BB)-EF1a-KRAB-dCas9-P2A-BlastR- Myosin IIB sgRNA3	This paper	N/A
pCRISPRi0010- Lenti-(BB)-EF1a-KRAB-dCas9-P2A-BlastR-ECT2 sgRNA2	This paper	N/A
Software and algorithms		
Fiji ImageJ	Fiji	https://fiji.sc/
GraphPad Prism 9	GraphPad	https://www.graphpad-prism.cn/
Adobe Illustrator	Adobe	https://www.adobe.com/cn/

RESOURCE AVAILABILITY

Lead contact

Further information and requests for resources and reagents should be directed to and will be fulfilled by the lead contact, Ting Gang Chew (tinggchew@intl.zju.edu.cn).

Materials availability

The plasmids generated in this study can be obtained from the lead contact upon request.

Data and code availability

- Microscopy data and protein blots reported in this study will be shared by the lead contact upon request.
- The paper does not report original code.
- Any additional information required to reanalyze the data reported in this paper is available from the lead contact upon request.

EXPERIMENTAL MODELS AND STUDY PARTICIPANTS DETAILS

Cell lines

MCF10A cell lines were cultured in DMEM F-12 (Shanghai BasalMedia) with Glutamax (Gibco), 5% horse serum (Biological Industries), 20 ng/mL EGF (Gibco), 0.5 mg/mL Hydrocortisone (MedChemExpress), 100 ng/mL Cholera toxin (Sigma), 10 μg/mL Insulin (Biological Industries), 1% Pen/Strep (Biological Industries) at 37°C with 5% CO2. The MCF10A cell line was a gift from Dr. Kuan Yoow Chan from Zhejiang University. The cells were authenticated by Sangon Biotech and were routinely checked for mycoplasma contamination in the lab using Myco-Blue

Mycoplasma Detector (Vazyme). MCF10A cells expressing mRuby2-AHPH and mEmerald-NMIIB, or dTomato-2xrGBD were prepared by lentivirus transduction and were enriched using the fluorescence-activated cell sorting (FACS). MCF10A cells expressing mEmerald-NMIIB WT, mEmerald-NMIIB S1935A, and mEmerald-NMIIB S1935D, mEmerald-NMIIB R709C, mEmerald-NMIIB R241A, mEmerald-NMIIB K647A, and all NMIIB double mutants, respectively, were prepared by lentivirus transduction and selected with 2 μg/mL puromycin (Sangon Biotech) and were enriched using the FACS. To knockdown endogenous NMIIB, the lentivirus expressing pCRISPRi0003 containing the guiding RNA (gRNA) targeting the NMIIB's 5′ UTR region was transduced into the cells expressing NMIIB mutants. Cells were selected with 6 μg/mL blasticidin (Solarbio) for 6 days and were continued to grow without the antibiotic for another 1 to 3 days before the experiments. To knockdown Ect2, the lentivirus expressing pCRISPRi0010 was transduced into cells.

METHOD DETAILS

Drug treatments

The following drugs were used in the study: NMII inhibitor: p-nitro-blebbistatin (Cayman Chemical, 24171); Rho inhibitor: C3 exoenzyme (Cytoskeleton, CT04); ROCK inhibitor: Y-27632 (MedChemExpress, HY-10583); CDK1 inhibitor: RO-3306 (Selleckchem, S7747). DMSO was used to dissolve p-nitro-blebbistatin, Y-27632 and RO-3306. C3 exoenzyme was dissolved in water. Details of concentrations used in the study are described in figure legends.

Lentiviral expression constructs

The following lentiviral transfer plasmids were used in the study: pTGL0427 containing mRuby2-AHPH in which AHPH was subcloned from an Addgene plasmid #68026 (a gift from Michael Glozter) and fused with mRuby2; pTGL0193 containing mEmerald-NMIIB, which was subcloned from an Addgene plasmid #54192 (a gift from Michael Davidson); pTGL0594 containing dTomato-2xrGBD subcloned from an Addgene plasmid #129625 (a gift from Dorus Gadella); pTGL0373 containing mEmerald-NMIIB S1935A; pTGL0374 containing mEmerald-NMIIB S1935D; pTGL0584 containing mEmerald-NMIIB R709C; pTGL0585 containing mEmerald-NMIIB R709C S1935D; pTGL0582 containing mEmerald-NMIIB R241A; pTGL0583 containing mEmerald-NMIIB R241A S1935D; pTGL0589 containing mEmerald-NMIIB K647A; pTGL0590 containing mEmerald-NMIIB K647A S1935D; pTGL0386 containing KRAB and dCas9 for CRISPRi (a gift from Jorge Ferrer, Addgene plasmid #118154); pCRISPRi0001 containing gRNA 5′ GTGCTAAAGGAGCCCGGCGG 3′ cloned into pTGL0386; pCRISPRi0002 containing gRNA 5′ GCTGGATCTGTGGTCGCGGC 3′ cloned into pTGL0386; pCRISPRi0003 containing gRNA 5′ GGACTGAGGCGCTGGATCTG 3′ cloned into pTGL0386; pCRISPRi0011 containing gRNA 5′ GGGCCGCCGGCGAGGAATGG 3′ (Ect2 knockdown). The 3rd generation lentiviral packaging system was used to prepare lentiviral particles. In brief, packaging plasmids pRSV-Rev, pMDLg/pRRE, pMD2.G (gifts from Didier Trono) were chemically transfected with the transfer plasmid into the 293Ta packaging cell line (Genecopoeia, LT008) using GeneTwin transfection reagent (Biomed, TG101). After 3 days, the culture medium was collected, filtered through a 0.45 μm filter, and then concentrated using the lentivirus concentration solution (Genomeditech, GM-040801) before adding to MCF10A cells.

Mitotic cell preparation

To increase the mitotic cell number, cells cultured on the imaging chambered coverglass were treated with 7.5 μM RO-3306 (Selleckchem) for 16 to 18 h at 37°C and were washed with the pre-warmed culture medium for 3 times to release cells into mitosis and added with 1 mL of fresh medium. Experiments were performed 40 min after the drug wash-off.

Elastic polyacrylamide gel preparation

The polyacrylamide gel used for cell compression was prepared as described in Matthews et al. and Le Berre et al. with modifications.[11,59] Briefly, 18 mm glass coverslips (Sangon, F518211) were treated with 10 μL Binding-silane (Sangon, C500226) for 10 min and then were rinsed with 100% ethanol and air-dried. To prepare soft elastic gels (2 kPa), 1 mL polyacrylamide gel solution was prepared by mixing 125 μL 40% w/v acrylamide (Sangon), 35 μL 2% bis-arylamide (Sangon), 10 μL APS (10% in water, Sangon), and 830 μL water. After adding and mixing 1 μL TEMED (Sangon) into the gel solution, about 350 μL of the final gel solution was immediately transferred onto a flat glass slide and covered by the coverslip pre-treated with the Binding-silane. After polymerization for 20 min, the gel and the attached coverslip were gently removed from the glass slide using a surgical blade and were soaked in PBS for at least 2 h and followed by incubation in cell culture media for overnight. In experiments that involved drug treatment, the gels were incubated in media containing the drugs for overnight.

Micropipette aspiration (MPA)

The micropipette was prepared by first pulling a borosilicate glass capillary (Sutter Instrument, B100-58-10) using the P-97 Micropipette puller (Sutter Instrument). Then, the thin end of a borosilicate glass capillary was cut by a Microforge (Narishige) to a diameter of about 5.5 μm. The micropipette was bent to a desired degree by heating it over an alcohol lamp and was filled with phosphate-buffered saline (PBS) using the MicroFil (World Precision Instruments, MF34G-5). The micropipette was installed to a micropipette holder, which was connected to a syringe pump (Harvard apparatus) and a 25 mL serological plastic pipettes via a three-way valve. The micropipette was positioned under an inverted microscope (Olympus, IX73) equipped with Olympus 60× objective lens (N.A. 1.35, U Plan super apochromat), a micromanipulator system (Eppendorf, TransferMan 4r), and a CMOS high speed camera (Vision Research, Phantom 410L, 333.33 nm/pixel).

To perform micropipette aspiration, cells were cultured on a one-well chambered coverglass (Cellvis, C1-1.5H-N) for 24 h and then were treated with 7.5 μM RO-3306 for 18 h. Cells were washed 3 times with fresh media and were added with fresh media containing 20 mM HEPES. Cells were incubated for another 40 min to reach mitosis. When a mitotic cell was aspirated by the micropipette, the microscopy image was captured and analyzed using Fiji to obtain the pipette radius (R_p) and the cell radius (R_c). The cell length of about half a diameter of the pipette opening was aspirated in. The water pressure changes (ΔP) as displayed on the 25 mL serological plastic pipette was also recorded. Cell surface tension (T) was then calculated based on the Laplace equation, $T = \Delta P/2 \, (1/R_p - 1/R_c)$.

Spinning-disk confocal microscopy for live-cell imaging

Spinning-disk confocal microscopy was equipped with a Nikon Eclipse Ti2-E inverted microscope, Nikon 60× oil-immersion objective lens (N.A. 1.40, Plan Apochromat Lambda), a spinning-disk system (Yokogawa Electric Corporation, CSU-W1), a Photometrics Prime 95B sCMOS camera, a Piezo Z stage (Physik Instrumente), and a live-cell stage top chamber with humidified CO_2 (Okolab). Images were acquired using the Metamorph with a z-step size of 0.5 μm and an x-y plane resolution of 183.33 nm/pixel. The fluorophores were excited by laser lines at wavelengths of 488, 561, or 640 nm. For experiments involving cell compression, a z stack of 30 μm was acquired before cells were compressed and a stack of 22 μm was acquired after cells were compressed. This ensured that the entire cell volume was covered during imaging.

Mitotic cell compression and live-cell imaging

To compress cells, 8 x 10^4 cells were first seeded on a 20 mm two-well chambered cover glass (Cellvis, C2-1.5H-N). Forty-eight hours later, cells were treated with 7.5 μM RO-3306 to synchronize cells at the G2/M boundary for 16 to 18 h. Prior to live-cell imaging with compression, synchronized cells were washed 3 times with the pre-warmed medium and added with 1 mL of fresh medium and incubated in the stage-top chamber attached to the spinning-disk microscopy for 40 min. When compressing the mitotic cells, the coverslip coated with the elastic gel was put over the cell layer and followed by a 5 g weight. Elastic gels and weights were pre-heated to 37°C in the chamber. In experiments where cells were treated with DMSO, 20 μM Y-27632 or 10 μM RO-3306, 1 mL medium containing 40 μM Y-27632 or 20 μM RO-3306 or containing equivalent volume of DMSO was added to cells grown in 1 mL medium on the chambered coverglass to achieve a final concentration of 20 μM Y-27632 or 10 μM RO-3306. The elastic gel that was pre-incubated with 20 μM Y-27632 or 10 μM RO-3306 for overnight was then put on top of the cell layer and followed by a 5 g weight. Cells at the same position were imaged before and after compression. The cell compression efficiency was validated by their decrease of cell heights. For microscopy imaging not involving cell compression, the μ-Slide 8-well chambered coverglass (ibidi, 80826) was used for cell culture and imaging. Mitotic chromosomes were labeled with 0.2 μM SiR-DNA in live cells during imaging (Cytoskeleton, CY-SC007).

Interphase cell compression

A 20 mm two-well chambered cover glass (Cellvis, C2-1.5H-N) was treated with 0.1 mg/mL polylysine for an hour and washed twice with PBS. Trypsinized MCF10A cells were then seeded to the treated chambered cover glass at the cell number of 2.5–3 x 10^4. The cells were left in the incubator for 4 to 5 h and were observed under a microscope. When cells started to attach to the cover glass bottom, 0.2 μM SiR-DNA (Cytoskeleton, CY-SC007) was added to cells to label DNA. Labeled cells were then compressed with coverslip coated with an elastic gel and a weight as performed in mitotic cells.

Image analysis and processing

Microscopy images were analyzed using Fiji. To quantitate fluorescence intensity of mEmerald-NMIIB, mRuby2-AHPH and dTomato-2xrGBD in mitotic cells (Figures 1C, 1F, S1E, and, S2A) and in mitotic cells for compression experiments (Figures 2E, 2F, 3B–3E, 4E, 5B–5D, and 6C), image stacks containing 5 slices around the mid-plane were projected along the z axis using the sum-intensity projection (Fiji/image/stacks/Z project). Background subtraction (Fiji/process/subtract background) was performed on projected images using the rolling ball radius of 20 pixels. Then, a segmented line with a line width of 4 (for mitotic cells) or 5 (for mitotic cells in compression experiments) was used to select the cortical fluorescent signals over the entire cell circumference. The mean fluorescence intensity of the selected line region from the same cells before and after treatment and/or compression was measured. The fold change was then calculated by dividing the intensity after treatment and/or compression to the intensity before treatment and/or compression. For time series in Figure 1B, the mean intensity of the cortical fluorescence was measured every 45 s. To quantitate the cell height in cell compression experiments, the number of slices from top to bottom of a cell were multiplied by 0.5 μm.

FRAP

FRAP was performed using the above-mentioned spinning-disk confocal microscopy equipped with Nikon 100× oil-immersion objective lens (N.A. 1.45, Plan Apochromat Lambda) and iLAS2 FRAP system (Gataca). Images were acquired using the Metamorph software at 110 nm/pixel. The mEmerald-NMIIB fluorescence signal was photobleached by using a short pulse of high power 488 nm laser lines and imaged by using a low power 488 nm laser lines. A small bleaching rectangular region of interest (ROI) of about 2 x 10-μm was drawn on the cortical mEmerald-NMIIB in mitotic cells. Three frames of pre-bleached images were acquired with 1 s interval before photobleaching, followed by time-lapse imaging of the same cells with 2 s interval for 120 s. The bleaching ROIs were recorded to locate the regions of bleaching during analysis.

Fiji was used to quantitate the fluorescence intensity of FRAP images. Background subtraction (Fiji/process/subtract background) was performed on the images with the rolling ball radius of 20 pixels. A segmented line ROI (line width 5) was used to select the FRAP regions for quantification. The mean intensity of ROIs for pre-bleached images and after bleached images ($I_{bleached}$) was calculated for each time point. A mean pre-bleached intensity ($I_{prebleach}$) was derived from the average of three pre-bleached images. The ratio of $I_{bleached}/I_{prebleach}$ at each time point was calculated and was subsequently deducted by the ratio of the first image after photobleaching to obtain $ratio_t$. The $ratio_t$ of each time point was plotted as the recovery curve and fitted using a non-linear fitting function (one-phase association function constrained by $Y0 = 0$ and plateau <1) in the Prism 9 software (GraphPad). The recovery time was derived from the half-time parameter calculated from the fitting. The mobile fraction was derived from the span parameter calculated from the fitting. The immobile fraction was calculated as a difference between 1 and the mobile fraction.

Cytoskeletal fractionation

Cells were washed once with ice-cold PBS. To a single well of a 6-well cell culture plate, 200 μL of lysis buffer (50 mM PIPES, pH 6.8, 46 mM NaCl, 2.5 mM EGTA, 1 mM $MgCl_2$, 1 mM ATP, 0.5% Triton X-100, protease inhibitor cocktail) was added. Lysates were harvested and centrifuged at 13000 g for 20 min at 4°C. The supernatant (soluble fraction) was separated from the pellet (cytoskeletal fraction). The pellet was then resuspended in a same volume of lysis buffer as the supernatant. Both fractions were added with 4 x LDS sample buffer (Genscript) and boiled for 5 min. The pellet suspension was sonicated in a water bath sonicator for 1 min with 20% power to improve solubility.

Protein immunoblotting

Protein samples were separated in a pre-cast SDS-PAGE gel (GenScript, M00657) and blotted to a PVDF membrane (EMD Millipore, immobilon-P, IPVH00010). Blots were blocked with 5% skim milk for 1 h at room temperature and were incubated at 4°C overnight with the NMIIB antibody (Proteintech, 19673-1-AP; used in Figures 4B, S5A and S5C) or the β-actin antibody (Genscript, A00702; used in Figures 4B and S1D) or the GFP antibody (HuaBio, ET1604-26; used in Figures 5B–5D and 6A) or GAPDH antibody (Cell Signaling Technology, #5174; used in Figure S5A) or p-MLC2 antibody (Cell Signaling Technology, #3675; used in Figure S1D). The secondary antibodies used were Alexa Fluor Plus 800-conjugated goat anti-rabbit IgG secondary antibody (ThermoFisher, A32735) and Alexa Fluor 680-conjugated goat anti-mouse IgG secondary antibody (ThermoFisher, A32729). Blots were imaged using the LI-COR Odyssey CLx imaging system. The signal intensity of protein bands was calculated using the LI-COR Image Studio software and Fiji. The cytoskeletal fraction was calculated by dividing the cytoskeletal fraction intensity by the sum intensity of cytoskeletal and soluble fractions. Protein band intensity measurements in Figure 4 were obtained from four proteins blots derived from four independent experiments. Protein band intensity measurements in Figures 5 and 6 were obtained from three proteins blots derived from three independent experiments. The protein lysate in Figure S1D was prepared using Minute Total Protein Extraction Kit for Animal Cultured Cells and Tissues (Invent Biotech, SD-001). Protein lysates used in protein blots in Figures 4, 5, and 6, and S5 were prepared using the cytoskeletal fractionation lysis buffer.

Quantitative real-time PCR (qPCR) for checking endogenous NMIIB

To validate the knockdown of endogenous NMIIB in cells used in Figures 4, 5, and 6, total RNAs were prepared from cells using the FastPure Cell/Tissue Total RNA Isolation Kit (Vazyme, RC101-01) and were reverse transcribed into cDNA using the HiScript II Q RT SuperMix for qPCR (Vazyme, R223-01). The expression level of cDNAs was determined using the real-time PCR with the ChamQ Universal SYBR qPCR Master Mix (Vazyme, Q711-02). The reaction mix was assembled on the hard-shell PCR plate (Bio-Rad, HSP9655), sealed with the Microseal 'B' seal (Bio-Rad, MSB1001), and was performed in the CFX96 Touch Real-Time PCR Detection System (Bio-RAD, C1000). Primers used in the qPCR: GAPDH, 5′ CAGGAGGCATTGCTGATGAT 3′ and 5′ GAAGGCTGGGGCTCATTT 3′; NMIIB, 5′ CCTCATGCTGACCTTGCAAA 3′ and 5′ GGACACAAAACCAATATTCCCATT 3′. The primer pair for NMIIB targets the 3′ UTR of NMIIB gene, allowing checking of endogenous NMIIB expression. The C_T value for GAPDH was used for normalization to obtain the relative expression level.

QUANTIFICATION AND STATISTICAL ANALYSIS

Statistical analysis was performed using Prism 9 (GraphPad). Datasets were analyzed by Student's t test. If datasets were not normally distributed, they were analyzed using the Mann-Whitney test. All graphs were plotted using Prism 9 (GraphPad). Statistical details can be found in the figure legends.